A Study of the Loop as a Compact Antenna

by

Andrew Lea

B.Eng., Dalhousie University, 2004

A THESIS SUBMITTED IN PARTIAL FULFILLMENT OF
THE REQUIREMENTS FOR THE DEGREE OF

MASTER OF APPLIED SCIENCE
in the School
of
Engineering Science

SIMON FRASER UNIVERSITY
2007

Your file Votre référence
ISBN: 978-0-494-40734-9
Our file Notre référence
ISBN: 978-0-494-40734-9

Approval

Name:	Andrew Lea
Degree:	Master of Applied Science
Title of Thesis:	A Study of the Loop as a Compact Antenna
Examining Committee:	Dr. Paul Ho Chair
	Dr. Rodney Vaughan Senior Supervisor
	Dr. James K. Cavers Supervisor
	Dr. Nima Mahanfar SFU Examiner
Date Approved:	April 11, 2007

Abstract

This thesis examines the suitability of the loop antenna for use as a compact radiating element. The derivation of the loop equation is reviewed, and a summary of the significant research on the electrically large loop antenna over the past century is presented. The theoretical radiation efficiency for the electrically large loop is derived. This analysis shows that the radiation efficiency of the loop antenna is drastically improved by increasing the electrical size of the loop. The theoretical input impedance is used to calculate the quality factor and bandwidth of the tuned loop antenna, and a suitable impedance matching technique is presented to attain this bandwidth. Several loop antennas were constructed, and a Wheeler cap was used to measure the radiation efficiency of these antennas. This measured radiation efficiency is shown to agree reasonably well with the theoretically predicted values.

Dedication

To my wife, Meghan, and father, James, both of whom asked everyday "when will the thesis be finished?", and whom will never read beyond these first two pages.

Acknowledgements

A thank you to my senior supervisor, Dr. Rodney Vaughan, who always had time to answer my questions, no matter what time of the day I knocked on his office door. I would also like to thank Dr. Nima Mahanfar for his suggestions and input during the latter part of this research.

Contents

Approval ii

Abstract iii

Dedication iv

Acknowledgements v

Contents vi

List of Figures viii

List of Tables xiii

1. Introduction 1

2. Existing Theoretical Analysis 4

   2.1 Loop Antenna Dimensions 4

   2.2 Small Loop Theory 5

   2.3 The Loop Equation 7

   2.4 Solving the Loop Equation 14

   2.5 Radiation Fields 17

3. Theoretical Results 18

   3.1 Current Distribution 18

   3.2 Radiation Efficiency 22

   3.3 Input Impedance 26

   3.4 Quality Factor, Bandwidth, and Impedance Matching 28

4. Loop Measurements 37

   4.1 Measured Impedances 39

4.2 Radiation Efficiency Measurements 43
5. A Compact Loop Design 49
5.1 Antenna Design Considerations 51
5.1.1 Printed Microstrip Loop versus Thin-Wire Loop 51
5.1.2 Optimum PCB Trace Width 54
5.1.3 Feed Structure 56
5.1.4 Coupling with Ground Plane 58
5.2 Predicted Tuned Bandwidth and Radiation Patterns 60
5.3 Matching Network Design 64
5.3.1 Matching Network Losses 67
5.4 Measurements 68
Conclusions 76
Appendices
A. Matching Network Loss Calculations 78
Bibliography 81

List of Figures

Figure 2.1: Thin-wire loop dimensions. 5

Figure 2.2: Small loop radiation efficiency for various loop thickness factors..... 7

Figure 2.3: Loop geometry for large radius vector, R. 10

Figure 2.4: Loop geometry for small radius vector, R. 10

Figure 3.1: Thin-wire loop current distribution from the Fourier series approximation and from the sinusoidal approximation for loop two ($\Omega = 10$)..... 19

Figure 3.2: First twenty Fourier coefficients, a_n, for loop two at two different electrical sizes. 20

Figure 3.3: Uniform cross-sectional current distribution. 20

Figure 3.4: Non-uniform cross-sectional current distribution for various loop thickness factors..... 22

Figure 3.5: Cross-sectional current distribution and skin depth for finite conductance loop conductor. 23

Figure 3.6: Theoretically derived radiation efficiency of the three theoretical loops. The radiation efficiency calculated using small loop theory is included for reference..... 25

Figure 3.7: Input admittance for the three theoretical loops calculated using the Fourier series current distribution..... 26

Figure 3.8: Input resistance for the three theoretical loops calculated using the Fourier series current distribution. 27

Figure 3.9: Input reactance for the three theoretical loops calculated using the Fourier series current distribution. 27

Figure 3.10: Input resistance comparison between small loop theory and an electrically large loop described using the Fourier series current expansion. 28

Figure 3.11: Tuned antenna with transmission line feed structure. 29

Figure 3.12: Theoretically predicted loop radiation quality factor. The fundamental limit (Chu) is included for comparison. 30

Figure 3.13: Theoretical tuned bandwidth for the three theoretical loop antennas. 31

Figure 3.14: Input reflection coefficient and bandwidth of the example tuned loop. 32

Figure 3.15: Two-element step-up matching network topology ($R_a > R_{in}$). 33

Figure 3.16: Composite structure: transmission line feed, two-element matching network, and tuned loop antenna. 34

Figure 3.17: Quality factor of the tuned loop and nodal quality factor of the matching network for the example loop antenna, loop two. 35

Figure 3.18: Input reflection coefficient of the tuned antenna with and without the additional matching network. 36

Figure 3.19: Composite structure with differential matching network and tuned antenna. 36

Figure 4.1: Half-loop impedance measurement setup. 37

Figure 4.2: Measured and theoretical input resistance for loop one ($\Omega = 8$). 39

Figure 4.3: Measured and theoretical input reactance for loop one ($\Omega = 8$). 40

Figure 4.4: Measured and theoretical input resistance for loop two ($\Omega = 10$). 40

Figure 4.5: Measured and theoretical input reactance for loop two (Ω = 10). 41
Figure 4.6: Measured and theoretical input resistance for loop three (Ω = 12). 41
Figure 4.7: Measured and theoretical input reactance for loop three (Ω = 12). 42
Figure 4.8: Dimensions of the Wheeler cap used to measure the loop antenna radiation efficiencies. 44
Figure 4.9: Measured input reactance of loop two in free-space and with the Wheeler cap. The measured frequency range is from 0.3 MHz to 2 GHz. 45
Figure 4.10: Measured input reactance of loop three in free-space and with the Wheeler cap. The measured frequency is from 0.3 MHz to 725 MHz. 45
Figure 4.11: Measured and theoretically predicted radiation efficiency for loop two (Ω = 10). The measured frequency range is from 0.3 MHz to 2 GHz. 46
Figure 4.12: Measured and theoretically predicted radiation efficiency for loop three (Ω = 12). The measured frequency is from 0.3 MHz to 725 MHz. 47
Figure 4.13: Measured and theoretical radiation efficiency for loops 2 and 3. The measured results are the fitted curves, not the raw data. 48
Figure 5.1: Final tag design with electronics and loop antenna. 49
Figure 5.2: Prototype antenna overview. 50
Figure 5.3: Finished prototype antenna. 51
Figure 5.4: Cross-sectional area comparison between thin-wire and a PCB trace. 53
Figure 5.5: PCB antenna dimensional restrictions. 54
Figure 5.6: Simulated radiation efficiency versus trace width for the PCB loop (from ADS Momentum) at a frequency of 915MHz. 56

Figure 5.7: Gap-Fed loop antenna and equivalent circuit including feed-gap capacitance. 57

Figure 5.8: Numerically simulated surface current on both the loop antenna and ground plane. A gap-voltage excitation is used. 59

Figure 5.9: Surface current induced on ground plane. 59

Figure 5.10: Simulated input resistance and input reactance. The lower and upper frequencies are 800 MHz and 1.0 GHz respectively. 60

Figure 5.11: Radiation quality factor calculated using the CST generated input impedance. The Chu (single mode) limit is included for reference. 61

Figure 5.12: CST simulated far-field pattern $G_{\phi}(\theta = 90°, \phi)$ for prototype antenna. 62

Figure 5.13: CST simulated far-field pattern for prototype antenna. The dashed line is $G_{\phi}(\theta, \phi = 90°)$ and the solid line is $G_{\theta}(\theta, \phi = 90°)$. 63

Figure 5.14: CST simulated far-field pattern cut $G_{\phi}(\theta, \phi = 0°)$ for prototype antenna. 63

Figure 5.15: Differential to single-ended matching network. 64

Figure 5.16: Series tuned loop antenna (single-ended). 65

Figure 5.17: Two-element step-down matching network topology (single-ended). 65

Figure 5.18: Single-ended discrete matching network. 66

Figure 5.19: Final matching network. 67

Figure 5.20: VNA measurement of antenna input impedance. 68

Figure 5.21: Measured loop input impedance and simulated CST input impedance. 70

Figure 5.22: Measured nodal impedance with $C_1 = 0.8$pF, $C_3 = 0.7$pF. The nodal impedance at 915 MHz (circled) is 6 + j27 ohms. 71

Figure 5.23: Measured nodal impedance with C_1 = 0.8pF, C_3 = 0.7pF, and C_2 = 5.0pF. The nodal impedance at 915 MHz (circled) is 166 + j5.3 ohms. 71

Figure 5.24: Measured input impedance of the antenna with complete matching network. The input impedance at 915 MHz (circled) is 43.2+ j8.8 ohms. 73

Figure 5.25: Measured return loss of the antenna with matching network. The return loss at 915 MHz (circled) is -18.5 dB. 73

Figure 5.26: Measured (dashed line) and simulated far-field pattern $|G(\theta = 90°, \phi)|$ for the prototype antenna. 74

Figure 5.27: Measured (dashed line) and simulated (solid line) far-field pattern $|G(\theta, \phi = 90°)|$ for the prototype antenna. 75

Figure 5.28: Measured (dashed line) and simulated (solid line) far-field pattern $|G(\theta, \phi = 0°)|$ for prototype antenna. 75

Figure 6.1: Theoretically derived radiation efficiency and maximum tuned bandwidth of a thin-wire loop antenna with radius of 20mm and loop thickness factor, Ω, of 10. 77

Figure A.1: Prototype antenna matching network 78

Figure A.2: Prototype antenna matching network 79

List of Tables

Table 2.1: Loop dimensions of the three theoretical loops. 5

Table 4.1: Loop dimensions of the three measured half-loops. 38

Table 4.2: Measured and theoretically predicted locations of the first anti-resonance in the loop input impedances. 42

Chapter 1

Introduction

Modern integrated circuit technology has advanced to the point where single chip digital transceivers can transmit power levels in excess of 10dBm and have receive sensitivities on the order of -115dBm[1]. These transceivers, combined with low-power microprocessors, form the building blocks of compact wireless tags capable of intra-tag communication over hundreds of meters. Tag to base-station ranges can be even greater with high-gain antenna arrays and more sophisticated digital signal processing available at the base-station. Examples of these systems include wireless sensor networks, implanted and external wireless medical devices, and wireless monitoring at home and in industry.

The battery and antenna are typically the limiting factors in the physical size of compact wireless tags. A compact antenna with high radiation efficiency maximizes the system performance while reducing demands on the battery, allowing further reduction in physical size.

The planar shape of the loop antenna makes it ideal for use as a compact antenna; however, like most other compact antennas, the electrically small loop suffers from poor radiation efficiency. Owing to this poor radiation efficiency, it has traditionally been

[1] Examples include Analog Device's AD7020 transceiver and Integration Associates' IA4420 transceiver.

limited to applications that are low-range, low data-rate communications or receive only systems such as pagers and AM radio.

The loop antenna is especially suitable for implanted wireless communications because its magnetic dominated near fields do not experience the same degree of tissue loading as do compact electric antennas.

This thesis examines the loop antenna as a compact antenna. It investigates how the radiation efficiency of a loop antenna is drastically improved by increasing the electrical size beyond the small loop threshold. The small loop threshold is normally defined by setting the normalized perimeter,

$$p_\lambda = \frac{p}{\lambda}, \tag{1.1}$$

where p is the perimeter of the loop and λ is the electromagnetic wavelength, to be one-third. The focus of this work is the region between the electrically small loop and the one-wavelength loop. The theoretical radiation efficiency at the upper end of this region will be shown to approach unity. The author has not been able to find previous work that specifically characterises this improvement in radiation efficiency.

Much information on the small loop antenna is readily available; however, it is of little use if an efficient antenna is needed, and most existing work on the electrically large loop antenna is overly academic and mathematically complex. A significant contribution of this work is extracting and assembling information beneficial to the practicing engineer from close to a century of academic study on the electrically large loop. Input impedance, appropriate impedance matching networks, and resulting tuned bandwidth are all considered.

Several thin-wire loops were built to confirm the predicted theoretical behaviour. Although rare, other authors have published measurements of the input impedance of electrically large loops. The radiation efficiency of these loops was also measured using

the Wheeler cap technique. Similar measurements of radiation efficiency are not available in the literature.

Finally, the development and testing of a compact loop antenna for use in a compact RF tag is covered, and the design of this antenna utilises many of the concepts from the other chapters. Measurements of input impedance, tuned bandwidth, radiation patterns, and radiation efficiency are presented and compared with predicted values from numerical simulations.

Chapter 2

Existing Theoretical Analysis

The first documented theoretical analysis of the electrically large thin-wire loop antenna is Pocklington's work (1897) who studied the receiving properties of such a loop [1]. Over a century has passed since this initial consideration of the electrically large loop, and in that time a huge amount of work has been contributed by many different authors; however, only a handful of these papers contribute a truly fundamental new development. The purpose of this chapter is to review key developments, and extract information relative to our interest in the compact loop antenna from previous work.

2.1 Loop Antenna Dimensions

Most of the academic work on the electrically large loop antenna is restricted to the thin-wire loop: a loop made from wire with a circular cross-section. The loop thickness factor,

$$\Omega = 2\ln\left(\frac{2\pi b}{a}\right), \tag{2.1}$$

is commonly used in the literature to quantify the relative thickness of the loop conductor to the radius of the loop, where the dimensions a and b are shown in fig. 2.1. The thickness factor and normalized perimeter completely describe the electromagnetic

radiation characteristics of the loop. Absolute dimensions are required only if ohmic losses need to be considered.

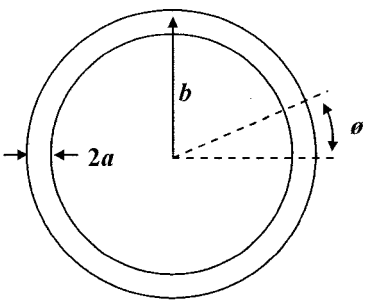

Figure 2.1: Thin-wire loop dimensions.

The three theoretical loops, given in table 2.1, are considered throughout the second and third chapters of this thesis. All three loops have the same perimeter, but a different thickness factor. Loop one, with a thickness factor of 8, is considered a thick-wire loop, whereas loop three, with a thickness factor of 12, is considered a thin-wire loop. These choices allow changes in loop thickness factor to be quantitatively analyzed independent from other parameters

Table 2.1: Loop dimensions of the three theoretical loops.

	a (mm)	b (mm)	p (mm)	Ω
Loop 1	2.3	20	125.7	8
Loop 2	0.85	20	125.7	10
Loop 3	0.31	20	125.7	12

2.2 Small Loop Theory

Small loop theory is well established and is covered in most of the classic introductory antenna textbooks [2], [3], and [4]. It assumes a uniform current distribution

along the length of the antenna, but as the frequency increases, the wavelength becomes comparable to the length of the antenna, and this assumption is no longer valid. Beyond this threshold the small loop equations no longer accurately describe the electromagnetic behaviour of the loop. The small loop threshold is generally accepted to be a normalized loop perimeter, p_λ, somewhere between one tenth and one third[2].

Small loop radiation resistance,

$$R_{rad} = 20\left(k^2 A\right)^2, \tag{2.2}$$

is dependent on only the wavenumber, k, and cross-sectional area, A, of the loop [3]. A more convenient form for a circular loop is obtained by expressing the area in terms of the normalized loop perimeter

$$R_{rad} = 20\left(\pi p_\lambda^2\right)^2. \tag{2.3}$$

The expression for ohmic loss,

$$R_\Omega = \frac{p}{2a}\sqrt{\frac{f\mu}{\sigma\pi}}, \tag{2.4}$$

is derived from skin depth equations [5]. Unlike radiation resistance, ohmic loss depends on the wavelength and the physical size of the loop, as shown by re-arranging (2.4)

$$R_\Omega = \frac{p_\lambda}{2a}\sqrt{\frac{\lambda c\mu}{\sigma\pi}}. \tag{2.5}$$

Radiation efficiency,

$$\eta = \frac{R_{rad}}{R_{rad} + R_\Omega}, \tag{2.6}$$

is expressed in terms of both ohmic loss and radiation loss.

---

[2] There is some disagreement amongst the classic antenna texts about the small loop threshold; Krauss gives 0.33, Stutzman gives 0.3, and Balanis gives 0.1 [2], [3], [4].

The resulting efficiencies of the three theoretical loops are shown in fig. 2.2. These curves are generated using small loop theory, and as previously discussed, become less accurate with increasing electrical size, particularly beyond the small loop threshold.

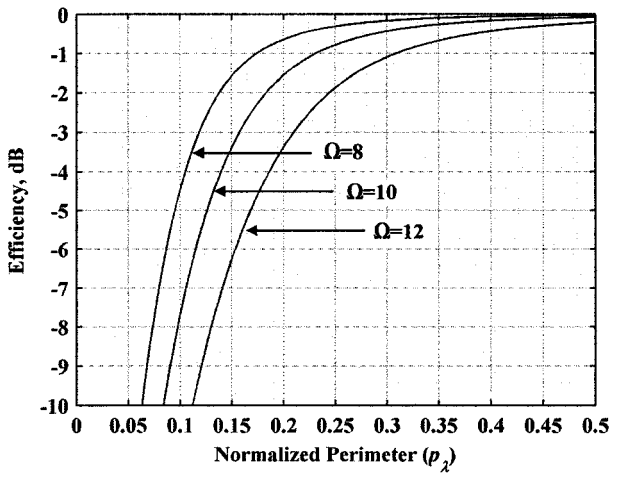

Figure 2.2: Small loop radiation efficiency for various loop thickness factors.

Fig. 2.2 highlights two important properties: first, increasing the thickness of the conductor reduces ohmic loss, and the overall efficiency improves; secondly, the small loop antenna is an extremely poor radiator.

2.3 The Loop Equation

Hallén (1938) was the first to consider an electrically large driven (transmitting) loop [6]. Using fundamental electromagnetic techniques he arrived at a single integral equation, the so called "loop equation", which completely describes the current on a thin-wire loop of arbitrary electrical size. His paper begins with Maxwell's equations and treats the loop as a special case of a more general problem, and as a result, the paper is lengthy and difficult to follow. Additionally, written almost 70 years ago, this paper uses a technical nomenclature significantly different than that in the modern literature making the mathematics even more difficult to follow.

With the loop equation, solving for current distribution on a thin-wire loop becomes essentially a mathematics problem. Most subsequent authors do not include a derivation of the loop equation, and instead use this equation as a starting point for further analysis. Some authors include the derivation, but offer only a compressed version that is difficult to follow without prior knowledge of the subject, and none convey all of the assumptions and simplifications necessary to fully understand the underlying electromagnetic principles. After reviewing the available literature, the author was unsatisfied with any of the available proofs and constructed the following proof with help from several sources from two pioneers of this field, R. P. W. King and S. Adachi [13], [16], [49].

The fundamental relation,

$$\vec{E}(\phi) = -\nabla\Phi(\phi) - j\omega\vec{A}(\phi), \tag{2.7}$$

where Φ is the electric potential and $\vec{A}$ is the vector magnetic potential, gives the electric field intensity at any point in space as the sum of contributions from electric current (via vector magnetic potential) and non-zero charge densities (via electric potential). For now, we are interested only in the electric field on the surface of the loop. This expression is the starting point for analysis of the thin-wire loop, and the bulk of the derivation is solving and manipulating the potential functions. Note that the electromagnetic variables are treated as time-harmonic phasor quantities.

The delta function generator is an electromagnetic abstraction commonly used to simplify the feed mechanism for the theoretical analysis of thin-wire antennas. It defines the electric field as zero everywhere along the surface of the antenna except across an infinitesimal gap at the feed, stated mathematically as

$$E_{\phi}(\phi) = -\frac{V_0\delta(\phi)}{b}, \tag{2.8}$$

where V_0 is the electric potential applied across the gap.

Several key assumptions must be stated before continuing. An ideal conductor is assumed, so all currents and free-charges are constrained to the surface of the loop. A thin-wire loop is assumed, where the thin-wire loop criteria is stated mathematically as $a^2 << b^2$ and $(ka)^2 << 1$. As a result, the surface current and free charge densities are both assumed to have uniform radial distribution around the cross-section of the conductor. Finally, the current is assumed to have only components in the phi, ø, direction.

The free-charge density, $\rho(\phi')$, can now be replaced with an equivalent charge per unit length, $q(\phi') = (2\pi a)\rho(\phi')$, and the surface current density, $\vec{J}(\phi')$, is replaced with total current, $\vec{I}(\phi') = (2\pi a)\vec{J}(\phi')$.

The electric (scalar) potential,

$$\Phi(\phi) = \frac{1}{4\pi\varepsilon}\int_{S'} \frac{q(\phi')}{2\pi a}\frac{e^{-jkR}}{R}dS', \tag{2.9}$$

is based on a differential surface instead of a differential volume, and requires evaluation of the radius, *R*, shown in fig. 2.3, from the elemental surface at ø′ to the observation point on the surface of the loop at ø. If the radius is much larger than the thickness of the loop, the latter can be neglected and the approximation

$$R \cong \sqrt{2b^2 - 2b^2\cos(\phi' - \phi)} = \sqrt{4b^2 \sin^2\left(\frac{\phi' - \phi}{2}\right)} \tag{2.10}$$

is used.

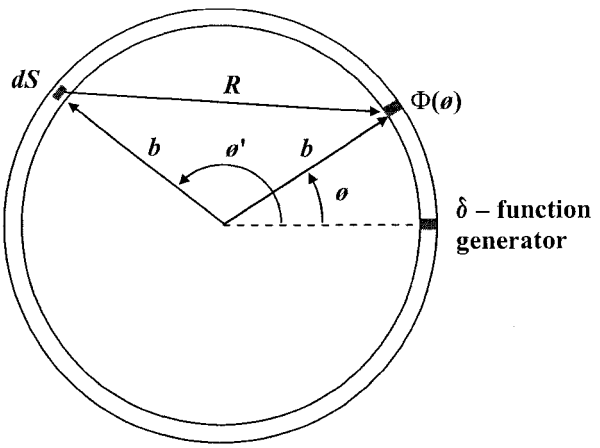

Figure 2.3: Loop geometry for large radius vector, *R*.

For small R, the loop can be approximated as illustrated in fig. 2.4.

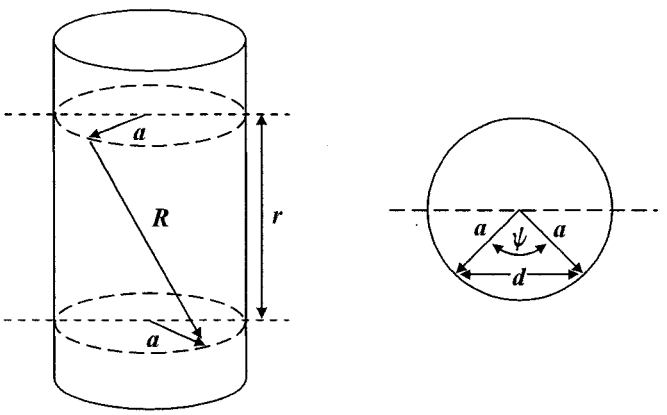

Figure 2.4: Loop geometry for small radius vector, *R*.

The curvature of the loop is ignored in this case, and the desired radius is the combination of two orthogonal components: $r = \sqrt{4b^2 \sin^2\left(\frac{\phi' - \phi}{2}\right)}$, and $d = \sqrt{4a^2 \sin^2\left(\frac{\psi}{2}\right)}$.

The resulting general expression

$$R \cong \sqrt{r^2 + d^2} = \sqrt{4b^2 \sin^2\left(\frac{\phi' - \phi}{2}\right) + 4a^2 \sin^2\left(\frac{\psi}{2}\right)} \tag{2.11}$$

is valid for both cases (small and large R), and the expression for electric potential is now

$$\Phi(\phi) = \frac{1}{4\pi\varepsilon} \int_{\phi'=-\pi}^{\phi'=\pi} \int_{\psi=-\pi}^{\psi=\pi} \frac{q(\phi')}{2\pi a} \frac{e^{-jkR}}{R} (a \cdot d\psi)(b \cdot d\phi'). \tag{2.12}$$

Note, the differential surface in (2.12) has been expanded as a product of two differential lengths.

The kernel function

$$W(\phi - \phi') = \int_{-\pi}^{\pi} \frac{b}{2\pi} \frac{e^{-jkR}}{R} d\psi \tag{2.13}$$

is commonly used in the literature, and simplifies the scalar potential as

$$\Phi(\phi) = \frac{1}{4\pi\varepsilon} \int_{\phi'=-\pi}^{\phi'=\pi} q(\phi') W(\phi - \phi') d\phi'. \tag{2.14}$$

The vector magnetic potential uses the same Green's function as the electric potential, but the magnetic potential is more complicated because of its vector nature.

The current vector at the differential surface, dS', is expressed in terms of the cylindrical unit vectors $I_{R'}(\phi')$ and $I_{\phi'}(\phi')$. The matrix identity

$$\begin{bmatrix} I_X(\phi') \\ I_Y(\phi') \end{bmatrix} = \begin{bmatrix} \cos\phi' & -\sin\phi' \\ \sin\phi' & \cos\phi' \end{bmatrix} \begin{bmatrix} I_{R'}(\phi') \\ I_{\phi'}(\phi') \end{bmatrix} \tag{2.15}$$

converts this current vector from cylindrical to cartesian coordinates, and the inverse matrix operation

$$\begin{bmatrix} I_R(\phi') \\ I_\phi(\phi') \end{bmatrix} = \begin{bmatrix} \cos\phi & -\sin\phi \\ \sin\phi & \cos\phi \end{bmatrix}^{-1} \begin{bmatrix} I_X(\phi') \\ I_Y(\phi') \end{bmatrix} \tag{2.16}$$

returns them to cylindrical coordinates - referenced now to unit vectors at the observation point at ø, not at the differential surface at ø'. Owing to the symmetry of the loop, only the ø component of vector potential,

$$A_\phi(\phi) = \frac{\mu}{4\pi} \int_{S'} \frac{I_\phi(\phi')}{2\pi a} \frac{e^{-jkR}}{R} dS', \tag{2.17}$$

needs to be considered. The ø component of the current is found from the matrix identities as $I_\phi(\phi') = \cos(\phi - \phi') I_{\phi'}(\phi')$, and the resulting magnetic potential is

$$A_\phi(\phi) = \frac{\mu}{4\pi} \int_{\phi'=-\pi}^{\phi'=\pi} I_{\phi'}(\phi') W(\phi - \phi') \cos(\phi - \phi') d\phi'. \tag{2.18}$$

Additional manipulations are needed before the potential functions can be substituted into the fundamental relation given in (2.7). The time-harmonic equation of continuity [43],

$$q(\phi') = \frac{j}{\omega b} \frac{\partial I_{\phi'}(\phi')}{\partial \phi'}, \tag{2.19}$$

relates electric charge to electrical current, and is used here to remove the surface charge distribution from the expression for electric potential

$$\Phi(\phi) = \frac{1}{4\pi\varepsilon} \int_{\phi'=-\pi}^{\phi'=\pi} \frac{j}{\omega b} \frac{\partial I_{\phi'}(\phi')}{\partial \phi'} W(\phi - \phi') d\phi'. \tag{2.20}$$

Equation (2.7) requires the partial spatial derivative of the electric potential. Leibitz's rule is used to find the derivative of the integral expression for electric potential

$$\nabla\Phi(\phi) = \frac{1}{b} \frac{\partial \Phi(\phi)}{\partial \phi} = \frac{j}{4\pi\varepsilon\omega b^2} \int_{\phi'=-\pi}^{\phi'=\pi} \frac{\partial I_{\phi'}(\phi')}{\partial \phi'} \left\{ \frac{\partial}{\partial \phi} W(\phi - \phi') \right\} d\phi'. \tag{2.21}$$

The identity $\frac{\partial W}{\partial \phi} = -\frac{\partial W}{\partial \phi'}$, provided by King, is used to re-arrange this differential expression,

$$\nabla\Phi(\phi) = -\frac{j}{4\pi\varepsilon\omega b^2}\int_{\phi'=-\pi}^{\phi'=\pi} \frac{\partial I_{\phi'}(\phi')}{\partial \phi'} \underbrace{\left\{\frac{\partial}{\partial \phi'} W(\phi-\phi')\right\}}_{g(\phi')} d\phi'. \tag{2.22}$$

Given the condition $I_{\phi'}(\phi')g(\phi')\Big|_{\phi'=-\pi}^{\phi'=\pi} = 0$, integration by parts reduces to

$$\int_{\phi'=-\pi}^{\phi'=\pi} \frac{\partial I_{\phi'}(\phi')}{\partial \phi'} g(\phi')\,d\phi' = -\int_{\phi'=-\pi}^{\phi'=\pi} I_{\phi'}(\phi')\frac{\partial g(\phi')}{\partial \phi'}\,d\phi', \tag{2.23}$$

and is used to rearrange (2.22) into a form more easily combined with the expression for magnetic potential (2.18)

$$\frac{1}{b}\frac{\partial\Phi(\phi)}{\partial\phi} = \frac{j}{4\pi\varepsilon\omega b^2}\int_{\phi'=-\pi}^{\phi'=\pi} I_{\phi'}(\phi')\left\{\frac{\partial^2}{\partial^2\phi'} W(\phi-\phi')\right\} d\phi'. \tag{2.24}$$

Finally, the free-space electromagnetic relations $\varepsilon_o = \frac{\mu_o}{\eta_o^2}$ and $\omega = \frac{\eta_o k_o}{\mu_o}$ are used to arrive at the familiar form of the loop equation

$$V_o\delta(\phi) = \frac{j\eta_o}{4\pi}\int_{\phi'=-\pi}^{\phi'=\pi} I_{\phi'}(\phi')\left[\frac{1}{k_o b}\frac{\partial^2}{\partial^2\phi'} + k_o b\cos(\phi-\phi')\right] W(\phi-\phi')\,d\phi'. \tag{2.25}$$

This integral equation completely describes the current distribution on the voltage driven thin-wire loop, and the only unknown is the current itself.

2.4 Solving the Loop Equation

The loop equation was first derived by Hallén. He was also the first to attempt to solve this equation using a Fourier series expansion to describe the current distribution

$$I(\phi) = \frac{-jV_o}{\eta_0 \pi}\left(\frac{1}{a_o} + 2\sum_{1}^{\infty}\frac{\cos(n\phi)}{a_n}\right). \tag{2.26}$$

The mathematical process of determining the current distribution, and in turn the Fourier coefficients, a_n, that satisfy the loop equation (2.25) is extremely difficult, and Hallén was unable to find an expression for the coefficients that resulted in a convergent series. Note that the Fourier coefficients, a_n, should not be confused with the wire radius, a.

Nearly twenty years later (1956), Storer was the first to successfully find a solution for the Fourier coefficients and numerically calculate the resulting current distributions and input impedance for various loops [7]. Once the current distribution is found, the input admittance, and input impedance, easily follows as

$$Y_{in} \equiv \frac{I(0)}{V_o} = \frac{-j}{\eta_0 \pi}\left(\frac{1}{a_o} + 2\sum_{1}^{\infty}\frac{1}{a_n}\right). \tag{2.27}$$

His approach truncated the series at five terms and replaced the rest of the terms with an equivalent integral.

In the same year, Kennedy published the first documented electrically large loop antenna input impedance measurements [8]. Using a half-loop over an image plane she measured the current distribution by physical probing and estimated the resulting admittance of a loop with thickness factor $\Omega = 11$. Despite admitted shortcomings in her impedance measurements, the measured conductance is in quite good agreement with Storer's theoretical value; however, there is a greater discrepancy between the measured and theoretical susceptances.

In 1962 T.T. Wu published what is now the accepted technique for determining the Fourier coefficients [9]. His brief paper questions the validity of Storer's approach, and presents an alternative mathematical procedure to obtain the Fourier coefficients, but does not calculate the resulting impedances. By considering the thickness of the conductor in more detail, Wu's derivation of the Green's function is more general than those previously considered.

King et. al released series of papers in 1963, 1964 and 1965 investigating the properties of a driven circular thin-wire loop immersed in a dissipative medium [10], [11], [12]. The second paper is the first to calculate current distributions and resulting impedances using Wu's approach. King calculated the admittance as a function of the number of Fourier terms to a maximum of twenty terms. His results showed that the conductance quickly converges with 8 terms included in the series; however, the susceptance continues to increase with the number of terms. The rate of increase is more pronounced for thicker loops ($\Omega < 10$) and for larger electrical sizes. He noted the conductance is very similar to Storer's results, which had already been shown to agree well with Kennedy's experimental data. The susceptance has more significant differences when compared with Storer's results, but the comparison isn't as meaningful since Storer's susceptance did not agree well with measurements.

King also made some key observations about the voltage delta-function generator which is purely a mathematical abstraction, and is unrealizable in practice. While it results in an accurate prediction of the current distribution and conductance, the infinitesimally small feed gap results in an infinite susceptance. As a result of the limitations of the delta-function generator, King makes the following conclusions on Wu's technique: "These results indicate that a Fourier Series solution in which 20 terms are retained is satisfactory for determining the admittance of thin-wire loops ($\Omega \geq 10$) that are not too large ($\beta d \leq 2.5$)"; and "The approximation is excellent for the conductance, somewhat less accurate for the susceptance".

G. S. Smith continued to work on loop antennas in homogeneous matter throughout the 1970s, and included some research on measuring the radiation resistance of loops with a wheeler cap [14], [15], [42]. Smith and King's work on loops in lossy matter are excellent references for embedded loop antennas [16]. This topic has recently showed renewed academic interest with the advent of surgically implanted wireless medical devices.

Interestingly, most of this research on loop antennas stems from Harvard University where Storer, King, Wu and Smith were all either faculty or graduate students.

In more recent literature, Zhou and Smith (1991) circumvent the susceptance problems associated with a delta-function generator by considering a coaxial fed loop antenna over an infinite image plane [18]. They model the coaxial feed as a magnetic frill which impresses a driving current onto a full loop and add a correction term to Wu's solution. Their measured impedances are in remarkable agreement with their theoretically predicted impedances.

Finally, the work of S. Adachi and Y. Mushiake should be included in this brief review. They published three papers in 1957 that formed a complete and concise analysis of the electrically large loop antenna. The first paper derives an alternate form of the loop equation [49], and following some simplifications, derives a closed form solution for the current distribution. The second paper calculates various electrical properties of the loop based on the current distribution obtained from the original paper [50], and the third paper considers a loop antenna parallel to a ground plane forming a more directional antenna [51]. Strangely, references to this work in the modern literature are scarce even though Adachi continued to publish research on the loop well into the 1970s.

2.5 Radiation Fields

This thesis does not examine theoretical expressions for the radiation fields of a loop antenna; however, much work has been done on the subject and a brief review of the available literature is included here.

The first authors to consider the radiation field of the electrically large thin-wire loop were Sherman (1944) and Glinski (1947) [19], [20]. Both authors used assumptions for the current distribution on the loop because these papers were published before the current distribution problem had been solved. Sherman assumed a sinusoidal current distribution, and Glinski used a transmission line as a model for the current distribution on a loop. Following these original papers, Martin (1960) expanded on the sinusoidal distribution, and Lindsay (1960) expanded on the transmission line model distribution [21], [22].

Rao (1968) was the first to numerically calculate the far-field patterns of the loop antenna using the Fourier series current distribution [23].

Much of the recent research on loop antennas deals with analytical calculations of the radiation field using the Fourier series current distribution [24], [25], [28], and in particular, exact expressions for the more complicated near-fields. This subject is of interest because of SAR (specific absorption rate) concerns with implanted antennas and antennas used in close proximity to the human body.

Chapter 3

Theoretical Results

The current distribution on a thin-wire antenna determines practically all other properties of interest such as input impedance, radiation efficiency, far-field patterns, and quality factor and tuned bandwidth. The King / Wu solution for the Fourier coefficients, a_n, is used throughout this chapter to describe the current distribution,

$$I_\phi(\phi) = \frac{-jV_o}{\xi_o \pi}\left(\frac{1}{a_o} + 2\sum_{1}^{19}\frac{\cos(n\phi)}{a_n}\right), \tag{3.1}$$

for the three loops presented in section 2.1. The expressions for the Fourier coefficients are tedious, and must be evaluated numerically. Readers are referred to several references for a succinct overview of the Fourier coefficient evaluation [9], [18].

3.1 Current Distribution

Fig. 3.1 shows both the Fourier series current distribution and the sinusoidal current distribution given by

$$I_\phi(\phi) = I_o \cos(kb(\phi - \pi)). \tag{3.2}$$

Both solutions result in a standing current wave around the loop with a maximum located 180 degrees from the feed location regardless of the electrical size of the loop. This maxima must be located at the mid-point of the loop to maintain a symmetric current distribution with respect to the feed location. Using the equation of continuity (2.19), this standing wave current distribution can be shown to produce a similar surface charge distribution.

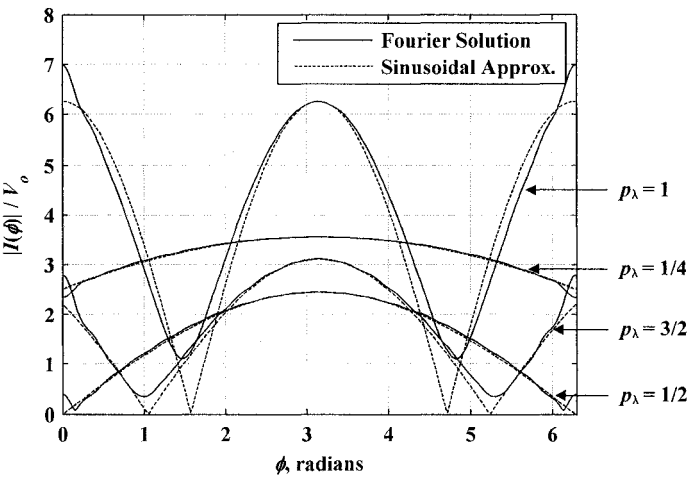

Figure 3.1: Thin-wire loop current distribution from the Fourier series approximation and from the sinusoidal approximation for loop two (Ω = 10).

The sinusoidal approximation and the Fourier series solution tend to differ at the driving point of the antenna. The input impedance is dependent on the current distribution at the feed of the antenna, so the sinusoidal approximation is not well suited to determining input impedances.

Fig. 3.2 shows the Fourier coefficients for the quarter wavelength loop, $p_\lambda = 1/4$, and the one wavelength loop, $p_\lambda = 1$. The fundamental component, a_1, is dominant for one wavelength loop, but for smaller loops the electrical size is less than the wavelength of this harmonic, and the uniform current component, a_0, is dominant.

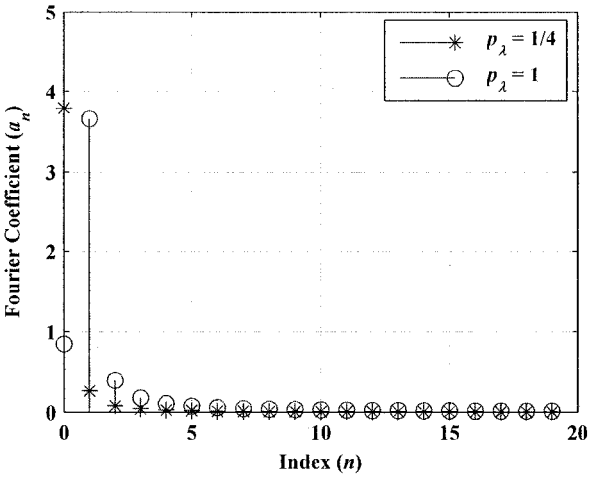

Figure 3.2: First twenty Fourier coefficients, a_n, for loop two at two different electrical sizes.

The thin-wire loop criteria was stated as $a^2 << b^2$ and $(ka)^2 << 1$, and accordingly the current is assumed to be uniformly distributed around the perimeter of the conductor as shown in fig. 3.3.

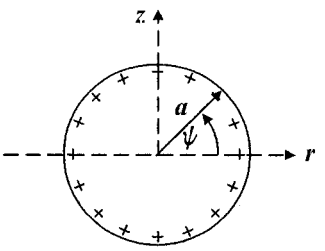

Figure 3.3: Uniform cross-sectional current distribution.

Balzano and Siwiak (1987) added a second dimension of basis functions, orthogonal to the plane of the loop, to the existing Fourier basis functions [17]. Using just two harmonics in this new direction, the distribution of the current around the cross-section of the conductor is investigated, and the thin-wire loop assumption is no longer required.

The current density is now a function of two angular dimensions ($\varnothing$, ψ)

$$J_{\phi}(\phi, z) = \sum_{n=-\infty}^{\infty} \sum_{q=-\infty}^{\infty} A_{n,q} e^{-jn\phi} F_q(z). \tag{3.3}$$

The two remaining assumptions are: first, the wire diameter is much smaller than one wavelength; and second, current is restricted to the phi direction.

Balzano constructed two loops, a thin-wire loop with thickness factor $\Omega = 11$, and a thick-wire loop with $\Omega = 9$. He measured the magnetic and electric field magnitudes in the vicinity of the loops and found that the measurements agreed reasonably well his theoretically calculated field strengths. Perhaps more interestingly, he observed from both theoretical analysis and measurements that the current density around the cross-section of the conductor varies approximately as $J_{\phi}(\phi,\psi) \approx J_{\phi}(\phi,b,\pm a) J_{\psi}(\psi)$, where the radial distribution around the cross-section of the wire,

$$J_{\psi}(\psi) = \frac{1}{1+\frac{a}{b}\cos(\psi)}, \tag{3.4}$$

is independent of the angle ϕ. Fig. 3.4 shows the cross-sectional current density distribution resulting from (3.4).

This relationship combined with the results of previous analysis gives

$$J(\phi,\psi) \approx \frac{I_{\phi}(\phi)}{2\pi a} \frac{1}{1+\frac{a}{b}\cos(\psi)}. \tag{3.5}$$

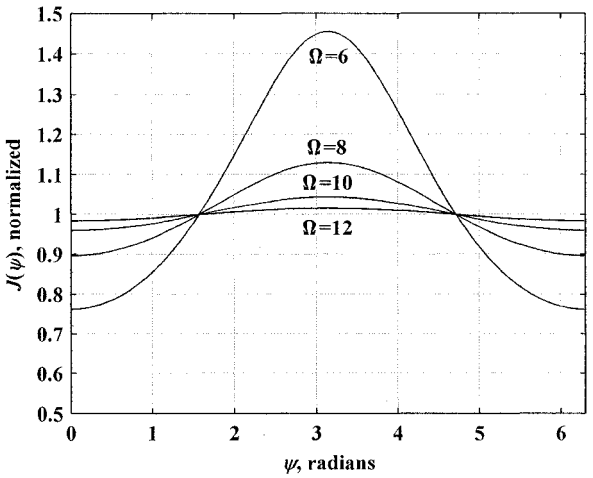

Figure 3.4: Non-uniform cross-sectional current distribution for various loop thickness factors.

The variation for the loops $\Omega = 10$ and $\Omega = 12$ is less than five percent and they can be classified as thin-wire loops. The loops less with a thickness factor less than 10 show more significant variation and should be classified as thick-wire loops. As the thickness factor increases, fig. 3.4 shows a concentration of current on the inside edge of the loop at $\psi = \pi$. This is an intuitive result because the inside edge provides the path of least inductance.

3.2 Radiation Efficiency

One of the primary drawbacks of the small loop antenna is poor radiation efficiency. The radiation efficiency of an electrically small loop can easily be calculated using small loop theory as in section 2.2; however, for an electrically large loop the Fourier series current distribution must be used. Additionally, if the loop doesn't qualify as a thin-wire loop, the cross-sectional distribution from section 3.1 must be considered.

The Fourier series current distribution was derived with the assumption of a lossless conductor, but finite conductance is inherently implied by considering radiation efficiency. A key initial assumption is that the finite conductivity of the loop material

does not significantly alter this distribution. This assumption should be valid for the highly conductive metals used in the construction of antennas.

The current is no longer restricted to the surface of the conductor, but is treated as having a uniform radial distribution from the surface of the conductor to a skin depth of

$$\delta = \sqrt{\frac{1}{\pi f \sigma \mu}}, \tag{3.6}$$

as is illustrated in fig. 3.5.

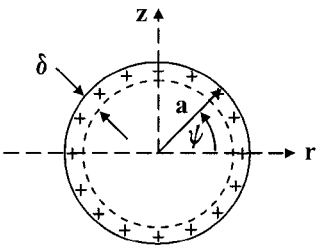

Figure 3.5: Cross-sectional current distribution and skin depth for finite conductance loop conductor.

The previously derived expressions for current density must be changed from a surface current (A/m) to an equivalent current density (A/m^2), and the resulting current density is

$$J(\phi,\psi) \approx \frac{1}{\delta}\frac{I_\phi(\phi)}{2\pi a}\frac{1}{1+\frac{a}{b}\cos(\psi)}. \tag{3.7}$$

The ohmic power loss is found by integrating the current density over the volume of the loop

$$P_\Omega = \frac{1}{2\sigma}\iiint_V \left|J(\phi,\psi)\right|^2 dV. \tag{3.8}$$

The differential volume in (3.8) can be expressed as $dV = \delta(a \cdot d\psi)(b \cdot d\phi)$, which allows the volume integral to be broken up into two independent one-dimensional integrals

$$P_{\Omega} = \frac{1}{2\sigma\delta(2\pi a)^2} \int_{\psi=0}^{\psi=2\pi} \frac{a \cdot d\phi}{\left(1+\frac{a}{b}\cos\psi\right)^2} \int_{\phi=-\pi}^{\phi=\pi} \left|I(\phi)\right|^2 b \cdot d\phi. \tag{3.9}$$

The first integral in (3.9) can be evaluated analytically, and the resulting expression for ohmic loss is

$$P_{\Omega} = \frac{1}{8\sigma\delta(\pi a)^2} \frac{1}{\left(1-\frac{a^2}{b^2}\right)^{3/2}} \int_{\phi=-\pi}^{\phi=\pi} \left|I(\phi)\right|^2 b \cdot d\phi. \tag{3.10}$$

The radiated power is found from the input impedance of the lossless loop,

$$P_{rad} = \frac{1}{2}\left|I_{in}^2\right|^2 R_{in}, \tag{3.11}$$

and the radiation efficiency is

$$\eta = \frac{P_{rad}}{P_{rad} + P_{\Omega}}. \tag{3.12}$$

Fig. 3.6 shows the radiation efficiency for the three theoretical loops calculated using (3.10) to (3.12) and the Fourier series current distribution. Small loop radiation efficiency is also shown for reference. Surprisingly, small loop theory provides a very good lower bound on radiation efficiency, even for the electrically large loop.

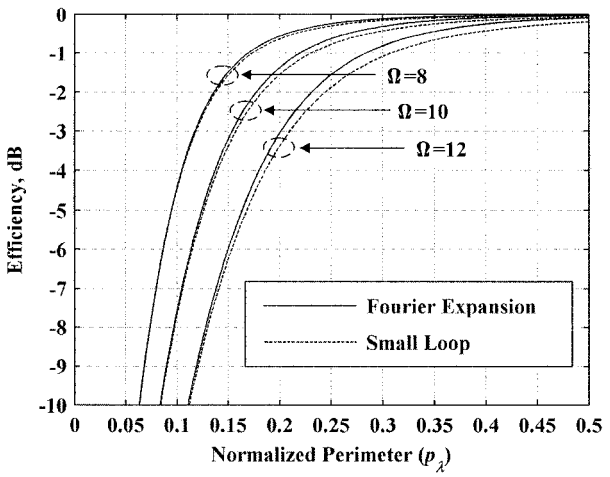

Figure 3.6: Theoretically derived radiation efficiency of the three theoretical loops. The radiation efficiency calculated using small loop theory is included for reference.

Clearly, the radiation efficiency of a small loop can be drastically improved by increasing the electrical size. Each of the loops considered here has an efficiency loss of less than -0.5 dB when the loop is half a wavelength in perimeter.

Radiation efficient at lower frequencies can be improved by using thicker loops. For example, a loop with thickness factor $\Omega = 8$ still shows good efficiency for a normalized perimeter, p_λ, of 0.2.

The PIFA (planar inverted F antenna) is the currently favoured low-profile compact element. The air substrate PIFA must have dimensions of roughly one-quarter wavelength by one-half wavelength, and requires a ground plane with dimensions of roughly one wavelength. As an alternative, consider a circular loop with perimeter of half-wavelength. The diameter of this circular antenna is $\frac{\lambda}{2\pi}$, demonstrating that the loop is hard to beat for an efficient and compact planar antenna.

3.3 Input Impedance

The input admittance is easily calculated from the Fourier series current distribution as given in (2.27). Fig. 3.7 shows the resulting input admittance for the three theoretical loops. The loop thickness factor influences both the conductance and susceptance. The rapid increase in conductance with electrical size reflects the conclusions from the previous chapter that as the electrical size increases the loop becomes a more effective radiator.

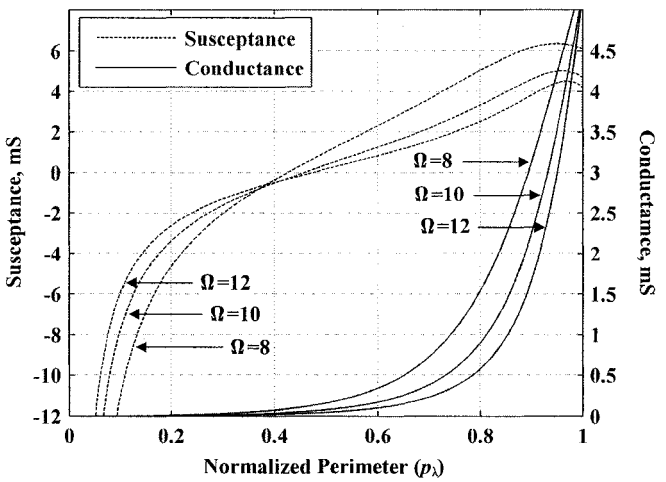

Figure 3.7: Input admittance for the three theoretical loops calculated using the Fourier series current distribution.

The input impedance of the three loops, shown in figs. 3.8 and 3.9, is calculated by taking the inverse of the admittance. The first anti-resonance occurs at a normalized perimeter of close to one-half, depending on the loop thickness factor, and the first resonance occurs near a perimeter of one wavelength. The location of both is important when considering impedance matching.

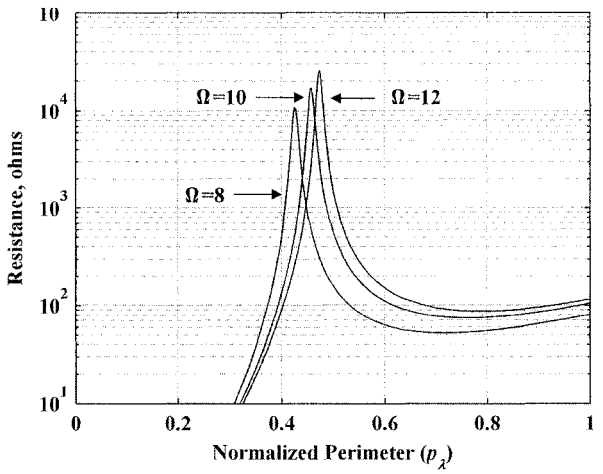

Figure 3.8: Input resistance for the three theoretical loops calculated using the Fourier series current distribution.

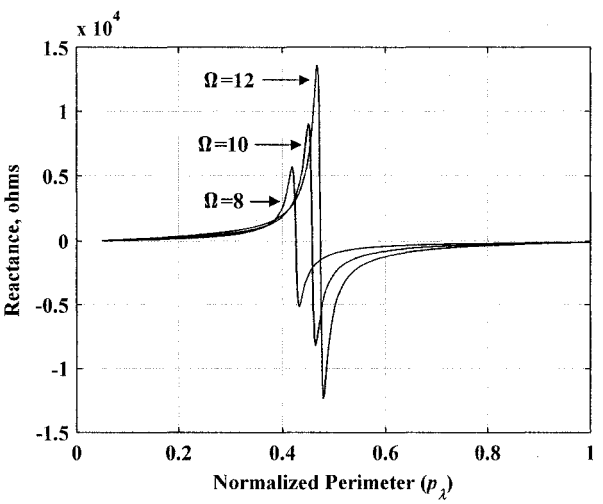

Figure 3.9: Input reactance for the three theoretical loops calculated using the Fourier series current distribution.

As previously mentioned in section 2.2, there is some disagreement about the location of the small loop threshold. One measure of this location is the difference between the small loop input resistance and the input resistance obtained from the Fourier series current expansion, shown in Fig. 3.10 for loop two.

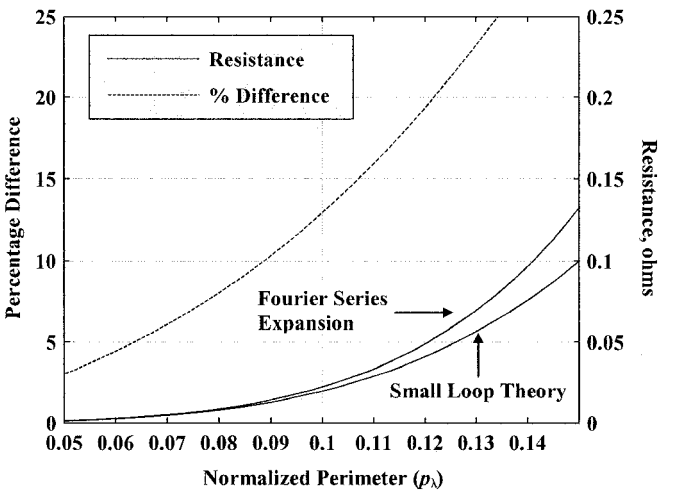

Figure 3.10: Input resistance comparison between small loop theory and an electrically large loop described using the Fourier series current expansion.

For a normalized loop perimeter of one-tenth of a wavelength, the difference between the two resistances is already greater than ten percent, suggesting for conservative estimates the lowest threshold (one-tenth of a wavelength) is appropriate.

3.4 Quality Factor, Bandwidth, and Impedance Matching

The quality factor, Q, in the context of antenna theory, is defined as the ratio of time averaged stored energy in the electric and magnetic near-fields to far-field radiated power

$$Q = \frac{\omega\left(W_m + W_e\right)}{P_{rad}}. \tag{3.13}$$

Quality factor is an important concept because it predicts the potential bandwidth of the resonated antenna, and is a convenient figure of merit to compare the performance of different antennas.

Best and Yaghjian have recently published a new technique to find the quality factor of the tuned antenna shown in fig. 3.11 [29]. The antenna is tuned to resonance with the lossless series matching element, $X_s(\omega)$, and here the loop input reactance is assumed to be capacitive, so the series reactive element is inductive. The tuned antenna is fed with a transmission line where $a_0(\omega)$ is the incident power wave and $\Gamma_0(\omega)$ is the input reflection coefficient. This approach solves problems experienced with previous techniques near anti-resonance frequencies, and since the loop antenna is anti-resonant at certain frequencies, this approach is well suited to the loop.

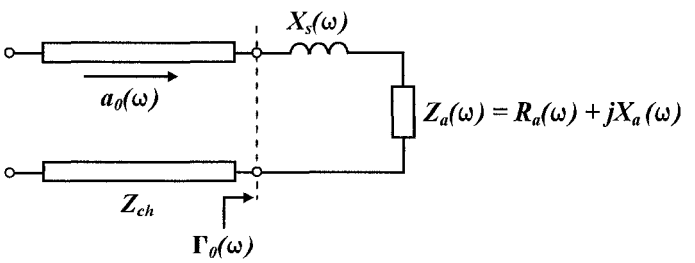

Figure 3.11: Tuned antenna with transmission line feed structure.

The quality factor is found from the input impedance of the tuned antenna

$$Q_z(\omega) = \frac{\omega}{2R_0(\omega)}\left|Z_0'(\omega)\right|. \tag{3.14}$$

The subscript z highlights that input impedance is used, whereas previous techniques used only the input reactance.

Fig 3.12 shows the tuned quality factor for three loops. The fundamental lower limit for a single-mode antenna,

$$Q = \frac{1}{(ka)^3} + \frac{1}{ka}, \tag{3.15}$$

is also shown [31]. The slight kink in the curves is an artefact of the numerical treatment.

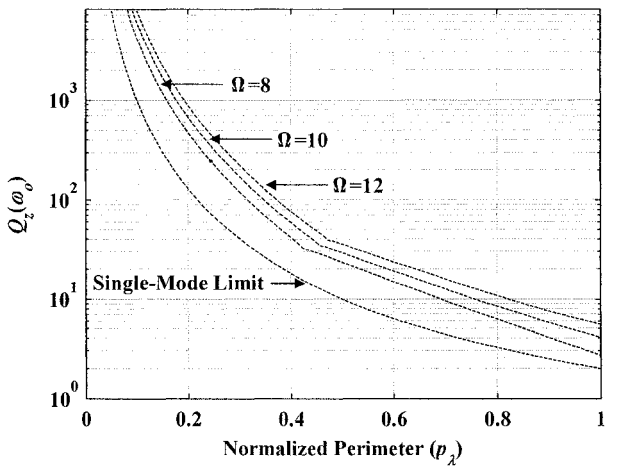

Figure 3.12: Theoretically predicted loop radiation quality factor. The single-mode fundamental limit is included for comparison.

The tuned quality factor in fig. 3.12 is for a lossless loop (infinite conductivity). A loop with finite conductivity will behave differently in the small loop region where the ohmic resistance is much greater than the radiation resistance.

The input power to the antenna is

$$P_{in} = \frac{1}{2Z_{ch}} \left| a_0(\omega) \right|^2 \left[1 - \left| \Gamma_0(\omega) \right|^2 \right]. \tag{3.16}$$

Best and Yaghjian, among others, showed that the half-power bandwidth of a tuned antenna, defined from the input reflection coefficient, can be approximated from the quality factor as

$$FBW_z \cong \frac{2}{Q_z}, \tag{3.17}$$

where FBW denotes fractional bandwidth normalized by the resonant frequency of the tuned antenna. This bandwidth definition assumes the characteristic impedance of the transmission line, Z_{ch}, is equal to the input resistance at resonance, $R_a(\omega_o)$, of the tuned

antenna, and presents a problem since 50 ohms is the generally accepted RF standard characteristic impedance.

Fig 3.13 shows the theoretical half-power fractional bandwidth predicted by (3.17) for three loop antennas.

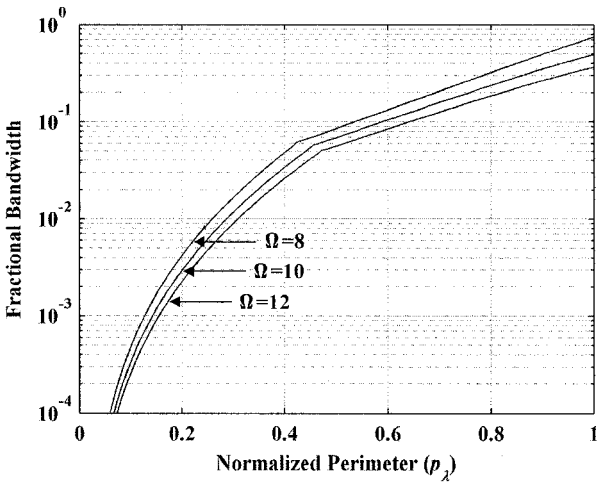

Figure 3.13: Theoretical tuned bandwidth for the three theoretical loop antennas.

The bandwidth of the antennas improves with increasing electrical size, and to a lesser extent, with increasing loop thickness factor.

To illustrate these concepts, consider loop two tuned to resonance at a normalized perimeter of 0.6, or equivalently 1.43GHz. The predicted input impedance is 110.7 – j791.4 ohms with a resonated quality factor of 19.0. Following (3.17), the predicted half-power bandwidth is 150.5MHz.

To confirm this prediction, fig. 3.14 shows the input reflection coefficient for the transmission line fed tuned antenna shown in fig. 3.11 with an 87.9 nH series inductor. This reflection coefficient was calculated numerically using the theoretical input impedance and simple circuit theory. Two characteristic impedances are considered: first, equal to the input resistance at resonance, $R_a(\omega_o)$; and second, 50 ohms. The graph

is a function of frequency instead of normalized perimeter to facilitate bandwidth estimates.

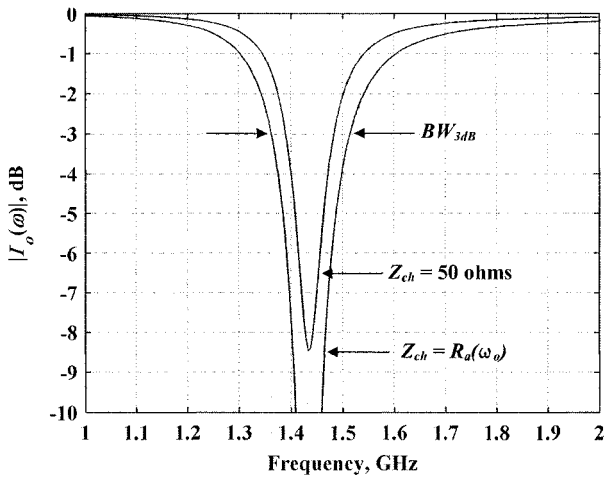

Figure 3.14: Input reflection coefficient and bandwidth of the example tuned loop.

The half-power bandwidth for the matched system, estimated from fig. 3.14, is 153MHz – very close to the predicted bandwidth of 150.5 MHz, and is considered the maximal bandwidth. The second curve shows significantly lower bandwidth as a result of the mismatch between the transmission line 50 ohm impedance and the input impedance of the tuned antenna. A matching network is needed to transform the tuned antenna input resistance to 50 ohms to optimize the bandwidth to that of the tuned system.

The motivation of this thesis is the loop as a compact element, so transmission line matching schemes are excluded since the required transmission line lengths would be similar to the overall length of the antenna. Discrete passive elements will introduce some ohmic loss into the system, but the improvement in power transfer and bandwidth, as well as the compactness, justify the additional loss.

Fig. 3.15 shows the topology for a two-element step-up matching network used when the input resistance of the antenna, R_a, is greater than the desired input resistance,

R_{in}, of 50 ohms. Reversing the order of the matching elements yields the step-down topology needed if the input resistance of the antenna is less than 50 ohms.

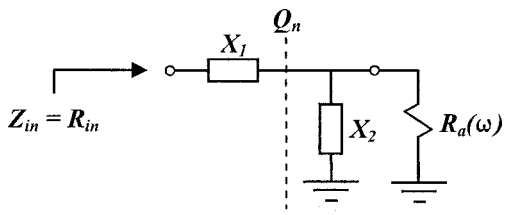

Figure 3.15: Two-element step-up matching network topology ($R_a > R_{in}$).

Design of the matching network begins with the impedance transform ratio,

$$n = \frac{R_a(\omega_0)}{R_{in}(\omega_0)}, \tag{3.18}$$

which determines all other parameters for a two-element matching network [35]. The concept of nodal quality factor, Q_n, is used extensively in matching network design [36], [37]. For a two-element matching network, the nodal quality factor is determined exclusively from the desired impedance transform ratio as

$$Q_n = \sqrt{n-1}. \tag{3.19}$$

Nodal quality factor is defined as the ratio between the reactive and real components of the unloaded input impedance at any node of a matching network,

$$\frac{|X_1|}{R_{in}} = \frac{R_a}{|X_2|} = Q_n, \tag{3.20}$$

and the reactance values, X_1 and X_2, follow from this definition.

The matching elements X_1 and X_2 must be opposite polarity, otherwise the choice is arbitrary. For this example the shunt element, X_2, is chosen to be capacitive, and the series element, X_1, is chosen to be inductive.

Fig. 3.16 shows the composite structure of a tuned antenna plus two-element matching network.

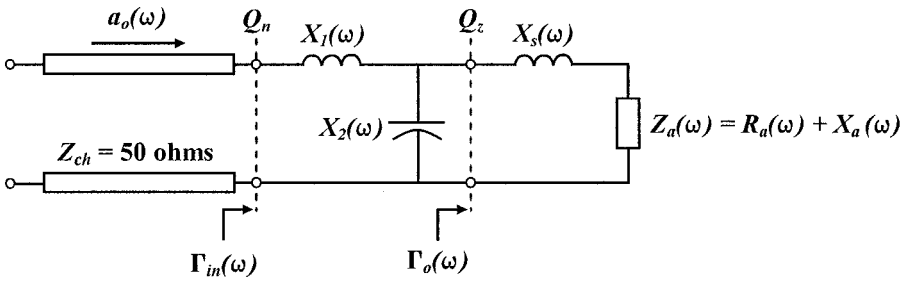

Figure 3.16: Composite structure: transmission line feed, two-element matching network, and tuned loop antenna.

The nodal quality factor also directly determines the half-power loaded bandwidth of a two-element matching network as

$$FBW = \frac{2}{Q_n}. \tag{3.21}$$

By adding additional elements, two at a time, this bandwidth can be increased; however, the improvement comes with a cost of increased ohmic loss inherently present in discrete components.

Following the procedure outlined above, the impedance transform ratio for the tuned loop (loop two) relative to 50 ohms is 2.2, the nodal quality factor is 1.1, and the required matching elements are a 6.1 nH series inductor and 1.1 pF shunt capacitor.

Note that both the nodal quality factor of the matching network (3.19) and the quality factor of the tuned antenna in (3.14) are a measure of unloaded quality factor, both fundamentally defined using the ratio of stored energy to dissipated energy, They can be directly compared to estimate the bandwidth of the composite structure as shown in fig. 3.17 for the example loop.

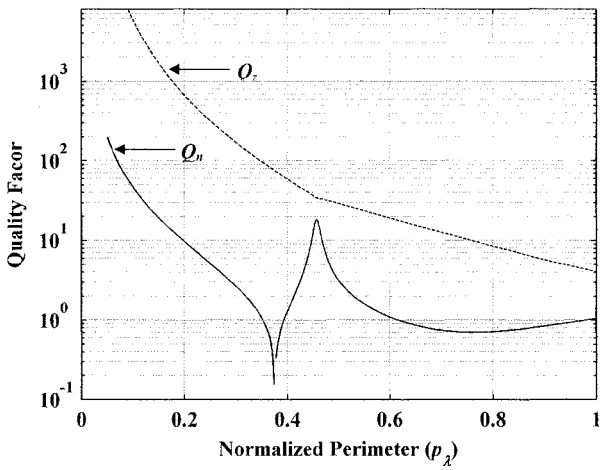

Figure 3.17: Quality factor of the tuned loop and nodal quality factor of the matching network for the example loop antenna, loop two.

The antenna quality factor is always the higher of the two, revealing that the tuned antenna is the limiting factor in bandwidth, not the two-element matching network.

Fig. 3.18 shows the reflection coefficients of the composite structure, $\Gamma_{in}(\omega)$, and the original tuned antenna, $\Gamma_o(\omega)$. As expected, the matching network has no significant effect on the bandwidth of the system. For this system, there is no advantage in using additional elements in the matching network.

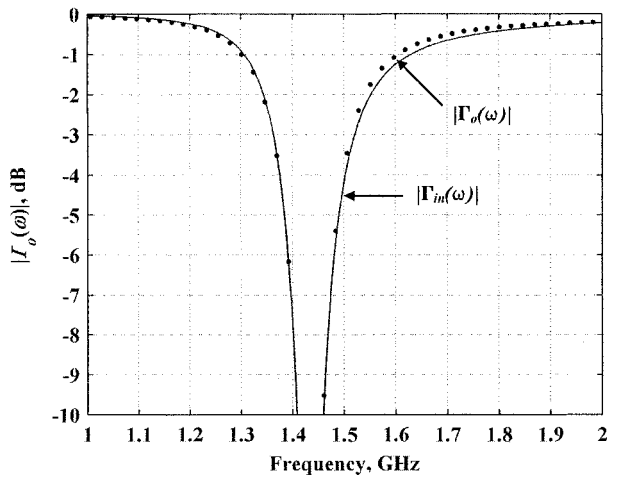

Figure 3.18: Input reflection coefficient of the tuned antenna with and without the additional matching network.

The loop antenna is a balanced system, which places additional practical implementation requirements on the matching network. The matching network can be re-distributed as shown in fig. 3.19 to achieve a balanced structure, where the input feed is also required to be differential.

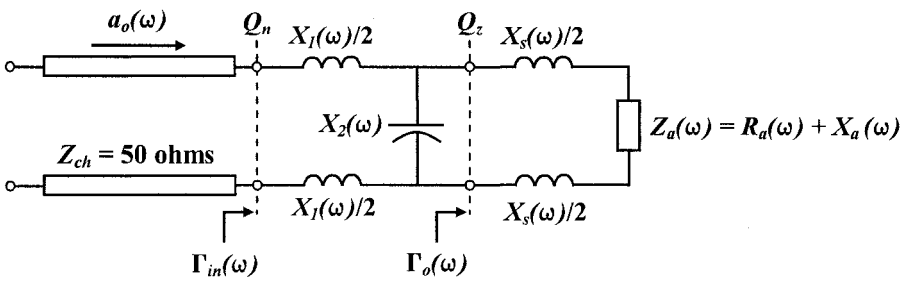

Figure 3.19: Composite structure with differential matching network and tuned antenna.

Chapter 4

Loop Measurements

The loop is a balanced antenna and must be fed differentially to maintain a symmetric current distribution. Modern vector network analyzers (VNA) connect to the device under test with unbalanced coaxial cable. A balun is needed to properly match the unbalanced coaxial cable to the balanced loop antenna, but most baluns are band-limited and will restrict the bandwith of the measurement. Additionally, depending on the type of balun employed, the effect of the balun on input impedance may be difficult to remove from the measurement.

A half-loop on an image plane (ground plane) is a popular alternative used widely in the literature because it provides an accurate measurement of the equivalent full loop input impedance while avoiding the complications of a balun [8], [18]. Three half-loops were built and measured using the set-up shown below in fig. 4.1.

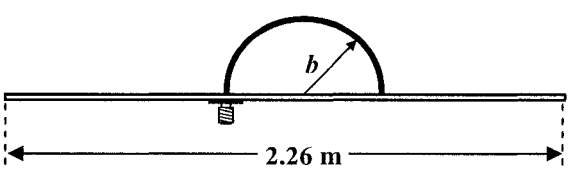

Figure 4.1: Half-loop impedance measurement setup.

The square image plane has length and width of 2.26 meters, and the antennas are fed from underneath the image plane with a flange mount SMA connector. The dimensions of the three loops are summarized in table 4.1.

Table 4.1: Loop dimensions of the three measured half-loops

	a (mm)	b (mm)	p (mm)	Ω
Loop 1	2.06	8.9	55.9	8
Loop 2	2.06	24.2	152.1	10
Loop 3	2.06	65.8	413.4	12

Table 4.1 gives the perimeter of the equivalent full loop. The three image plane loops cover the same span of thickness factor as the previous three theoretical loops. The previous loops were all the same perimeter, and the diameter of the wire was varied to achieve the desired loop thickness factor. To facilitate construction, the image plane loops are built from the same gauge wire, and the perimeter of the loops is varied to achieve the desired loop thickness factor.

The input impedance of the equivalent full loop is related to the impedance of the half-loop by

$$Z_{loop}(\omega) = 2 \cdot Z_{half-loop}(\omega). \tag{4.1}$$

There will be some diffraction effects in the measured impedance caused by the finite image plane. When considering this diffraction, a circular image plane represents the worst case scenario as the distance from the antenna to the edge of the image plane is constant all around the perimeter of the image plane. As the wavelength decreases, the measured impedance oscillates and asymptotically approaches the impedance of with an infinite image plane. This distance is not constant for the square image plane and will help to average this diffraction effect.

The following VNA settings were used to obtain accurate measurements of the untuned loops: 10 dBm output power, 10 kHz IF bandwidth, and time averaging factor of 50. These settings maximise the signal to noise ratio (SNR) of the measurements.

4.1 Measured Impedances

Figs. 4.2 to 4.7 show the measured impedance of each of the three loops, and also the theoretical impedance as calculated using the twenty term Fourier series expansion.

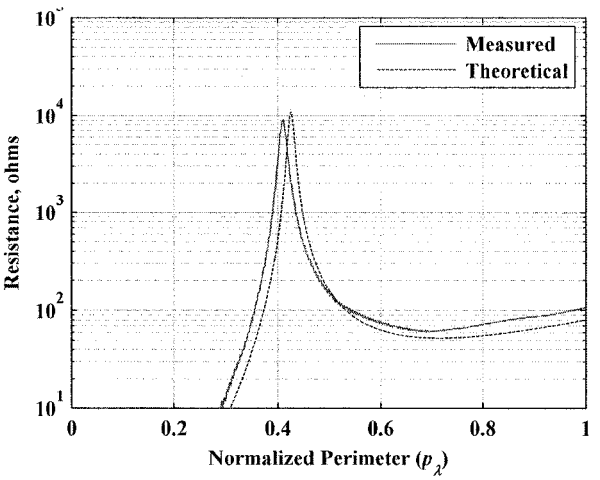

Figure 4.2: Measured and theoretical input resistance for loop one (Ω = 8).

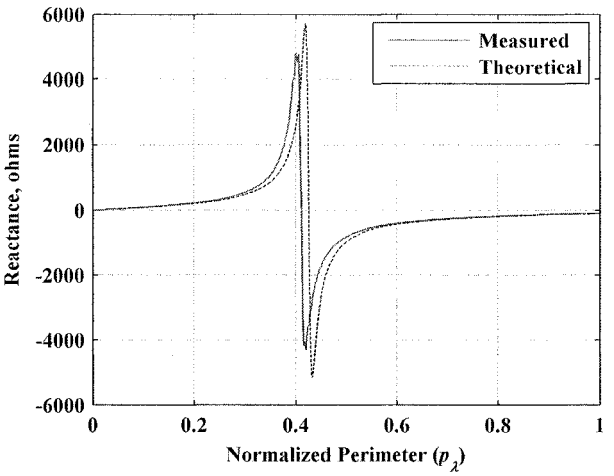

Figure 4.3: Measured and theoretical input reactance for loop one (Ω = 8).

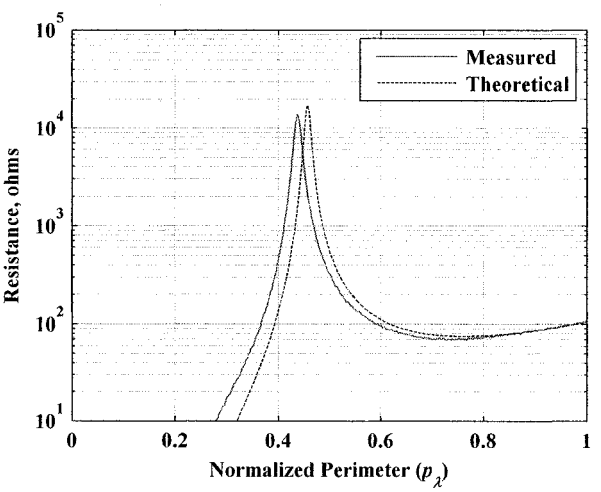

Figure 4.4: Measured and theoretical input resistance for loop two (Ω = 10).

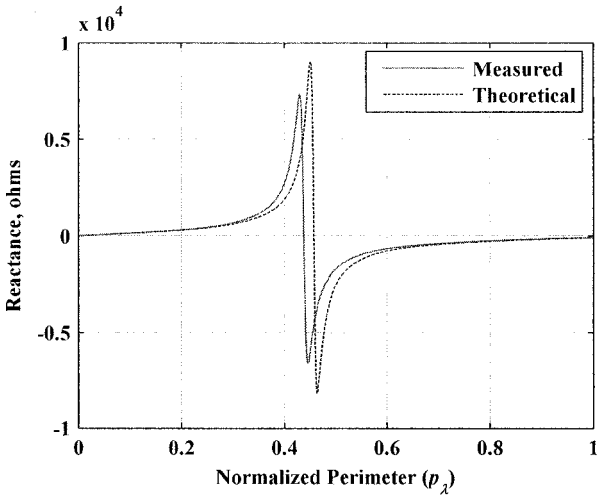

Figure 4.5: Measured and theoretical input reactance for loop two (Ω = 10).

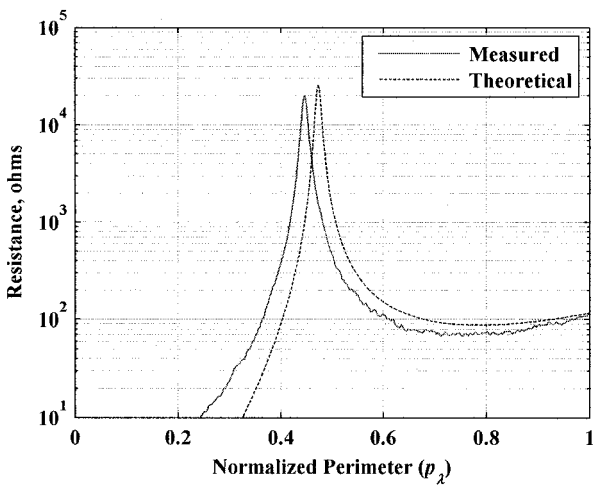

Figure 4.6: Measured and theoretical input resistance for loop three (Ω = 12).

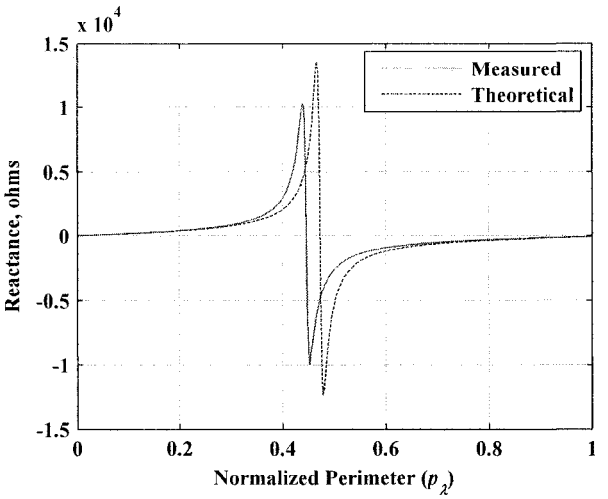

Figure 4.7: Measured and theoretical input reactance for loop three (Ω = 12).

In general, the measured impedances agree well with the theoretically predicted impedances; however, the anti-resonance in each of the measurements occurs at a slightly lower frequency than predicted, as summarised in table 4.2.

Table 4.2: Measured and theoretically predicted locations of the first anti-resonance in the loop input impedances.

	Ω	Measured f_0	Theoretical f_0	Percentage difference
Loop 1	8	2202 MHz	2283 MHz	-3.5 %
Loop 2	10	863.2 MHz	901.7 MHz	-4.3 %
Loop 3	12	323.8 MHz	343.2 MHz	-5.6 %

Since this resonance shift is similar in all three of the antennas it is probably a systematic effect and not a random deviation. It is likely caused by the difference in feed structure used in the theoretical analysis and the measurement setup. The theoretical analysis uses a delta function generator whereas the measured loops are driven with a coax cable. Smith and Zhou have presented a modified calculation of the Fourier

coefficients based on this type of feed structure that could potentially yield more accurate agreement [18]; however, this is not pursued further here.

4.2 Radiation Efficiency Measurements

A Wheeler cap was used to measure the radiation efficiency of two of the loop antennas. This approach was originally proposed by Wheeler, and several well known authors have evaluated this technique both theoretically and experimentally [40], [41], [42]. The consensus amongst these papers is the technique is generally easier to implement than alternative approaches, and it is well suited to comparing relative efficiencies, but is not highly accurate for measuring absolute efficiency.

The antenna radiation efficiency is determined by first measuring the input resistance of the antenna in free-space, R_1. The antenna is then enclosed in a conductive chamber and the input resistance is measured again, R_2. Ideally, the conductive chamber returns all radiating power to the antenna, removing the radiation resistance from the second measurement, and the radiation efficiency is found as

$$\eta = \frac{R_1 - R_2}{R_1}. \tag{4.2}$$

The Wheeler cap must not distort the current distribution or near-fields of the antenna. Accordingly, Wheeler suggested the distance between the antenna and cap must be at least one radiansphere,

$$r = \frac{\lambda}{2\pi}, \tag{4.3}$$

generally accepted as the boundary between the near-fields and far-fields of an antenna. The shape of the cap is not critical as long as this condition is met.

The Wheeler cap built to measure the radiation efficiency of the half-loop antennas is shown in fig. 4.8. It was constructed by building a cardboard box of appropriate size and then lining the box with aluminium foil. It was not expected to

produce highly accurate results, but instead to verify predicted trends. The cap can accommodate an antenna with radiansphere of less than 0.5 meters. This size was chosen so the efficiency of loop two could be measured down to a normalized perimeter, p_λ, of 0.05 where this antenna's radiansphere is 0.48 meters. The largest loop, loop three, has a radiansphere of 0.5 meters at a normalized perimeter of 0.13. Measurements below this electrical size will result in a radiansphere larger than the cap dimensions and must be treated with caution.

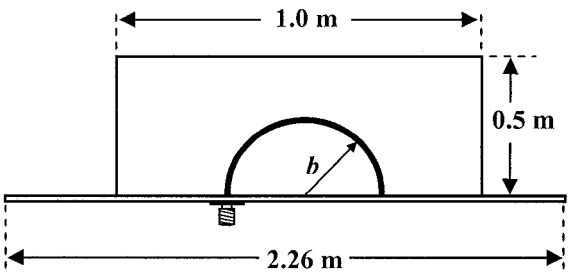

Figure 4.8: Dimensions of the Wheeler cap used to measure the loop antenna radiation efficiencies.

The input reactance of an antenna is determined exclusively by the antenna's near-fields, so the measured input reactance should be unchanged by the cap. Figs. 4.9 and 4.10 show the measured input reactance of loops two and three with and without the cap.

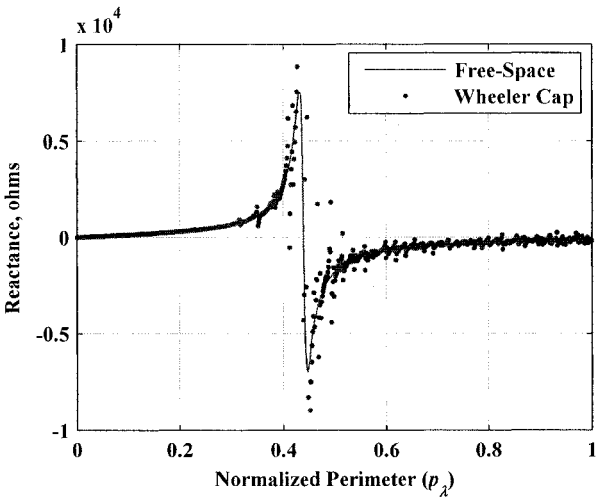

Figure 4.9: Measured input reactance of loop two in free-space and with the Wheeler cap. The measured frequency range is from 0.3 MHz to 2 GHz.

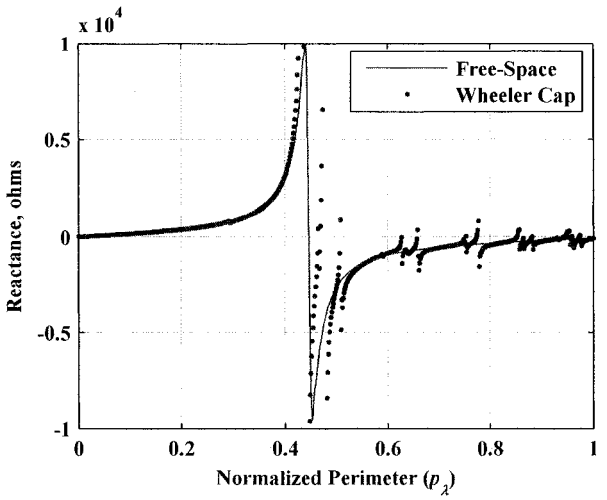

Figure 4.10: Measured input reactance of loop three in free-space and with the Wheeler cap. The measured frequency is from 0.3 MHz to 725 MHz.

The rectangular Wheeler cap forms a very effective resonant cavity, which can be problematic. In the literature, Wheeler caps are typically used to measure the efficiency of tuned antennas at the resonant frequency of the antenna. The radius of the cap is generally set close to one radiansphere at this frequency, well below the cutoff frequency

of the lowest resonant mode, and the resonant nature of the cavity does not interfere with the measurements.

Here, as the wavelength is reduced, the measurements sweep through many cavity resonant modes at frequencies determined by the geometry of the cap. These strong resonances are clearly present in the measured reactance of fig 4.9 and fig 4.10. The larger loop (loop three) is measured at lower frequencies, where the resonant modes are spaced further apart compared to the smaller antenna (loop two). Other than the effect of the resonant modes, the measured reactances are mostly unchanged by the cap.

Figs. 4.11 and 4.12 show the measured radiation efficiency for loops two and three. Again, the resonant cavity modes are spread further apart for the larger loop; however, the trend in efficiency is clearly visible, and an exponential curve fit is included in both figures. The theoretically predicted efficiency, evaluated numerically with the approach outlined in section 3.2, is also shown for comparison.

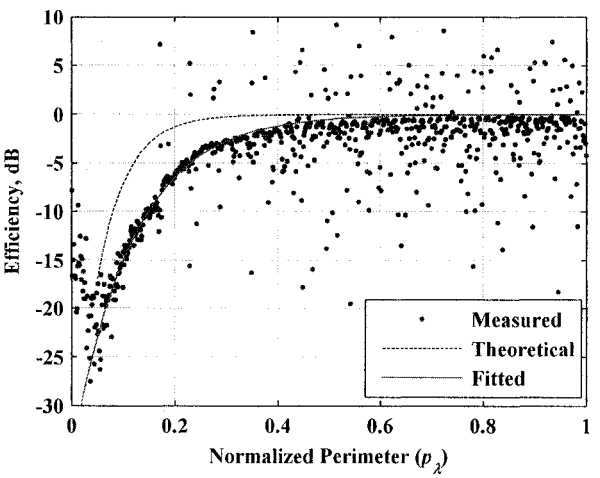

Figure 4.11: Measured and theoretically predicted radiation efficiency for loop two (Ω = 10). The measured frequency range is from 0.3 MHz to 2 GHz.

It should be emphasized that the apparent error in these measurements is not a random error, but is a deterministic measurement system error caused by the losses

(ohmic and radiation leakage) of the Wheeler cap. The measurements were taken several times and the scattered data points were the same each time.

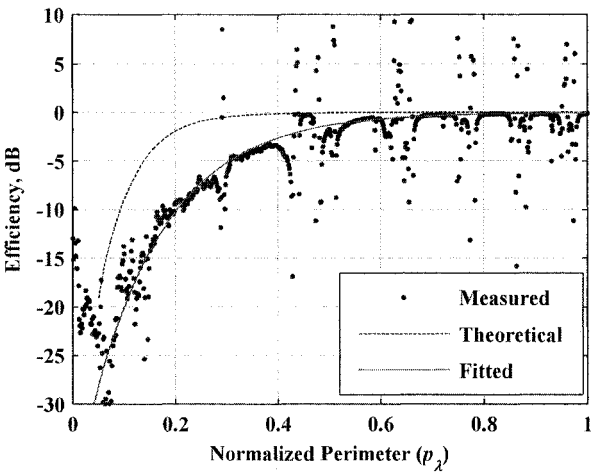

Figure 4.12: Measured and theoretically predicted radiation efficiency for loop three (Ω = 12). The measured frequency is from 0.3 MHz to 725 MHz.

The measured efficiency of both loops is lower than expected at intermediate electrical sizes, but asymptotically approaches the predicted efficiency with increasing electrical size. The Wheeler cap will have ohmic losses and radiation losses at the seams of the aluminium foil and at the boundary between the ground plane and the cap. Following Smith [42], these losses, R_c, will degrade the measured efficiency,

$$\eta = \frac{R_1 - R_2}{R_1} = \frac{R_{Rad} - R_{Cap}}{R_{Rad} + R_\Omega}, \tag{4.4}$$

where R_Ω and R_{Rad} are the antenna ohmic loss and antenna radiation resistance respectively. As the electrical size increases the radiation resistance becomes much larger than both the antenna ohmic loss and cap loss, and the efficiency approaches unity.

Fig. 4.13 shows the fitted measurement results and the theoretical efficiency.

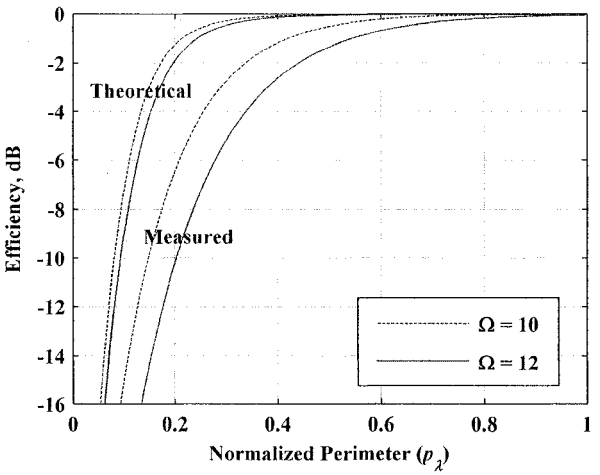

Figure 4.13: Measured and theoretical radiation efficiency for loops 2 and 3. The measured results are the fitted curves, not the raw data.

As predicted, increasing the loop thickness factor increases the radiation efficiency of the antenna. The losses of the cap need to be accounted for to produce a more precise measurement of absolute efficiency, but estimates of these losses are not attempted in this thesis. Two authors have concluded that the ohmic loss in a metal cap has a negligible affect on the measured efficiency [42], [40], so the primary source of additional loss in the measurements is expected to be leakage radiation.

Chapter 5

A Compact Loop Design

This chapter summarizes the design and testing of a loop antenna for a use in a compact wireless tag. The goal of this design is to maximize the radiation efficiency of the antenna, which will optimize both the communications range and the battery lifespan of the tag. The bandwidth and radiation efficiency of the antenna and associated impedance matching are all optimized based on the theoretical analysis of the previous chapters. The communications link is binary FSK at a carrier frequency of 915 MHz and a maximum data rate of 50 kbps. The required bandwidth of this link is approximately 150 kHz.

The tag electronics and antenna are located on a rectangular printed circuit board (PCB) as shown in fig. 5.1.

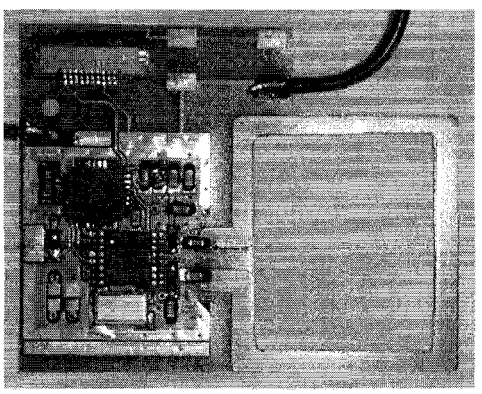

Figure 5.1: Final tag design with electronics and loop antenna.

A rectangular printed loop antenna, extending around the perimeter of the space available for the antenna, maximizes the electrical length and radiation efficiency of the antenna. The tag electronics are located on the left hand side of the PCB, and a ground plane is located on the bottom side of the PCB under the electronics.

A prototype antenna was built to measure the antenna input impedance and radiation patterns, and to aid in developing the impedance matching network. The dimensions of the prototype antenna are shown below in fig. 5.2.

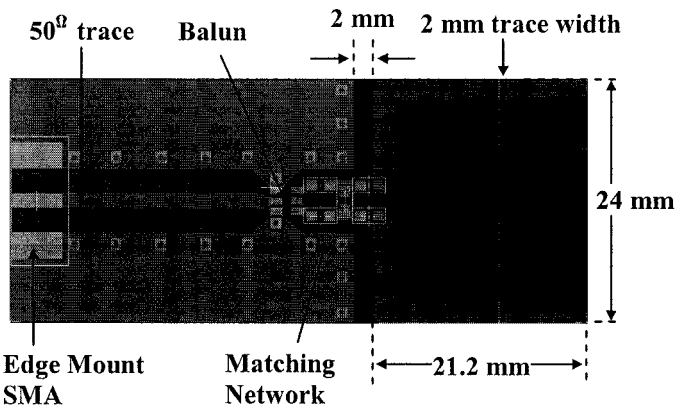

Figure 5.2: Prototype antenna overview.

A matching network of discrete surface mount components transforms the balanced (differential) antenna impedance to 50 ohms unbalanced (single-ended). No electronics are included on the prototype antenna. Instead, the input of the matching network is fed to an edge-mount SMA connector via a 50-ohm microstrip transmission line.

A picture of the final prototype antenna is shown in fig. 5.3. The copper tape on the sides of the PCB ensures a low impedance RF path between the ground plane on the top and bottom layers of the board.

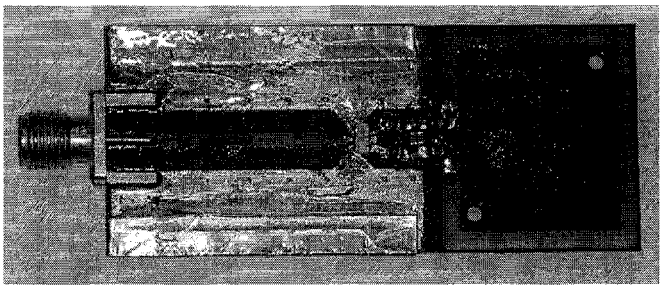

Figure 5.3: Finished prototype antenna.

Two numerical packages, CST's Microwave Studio and Agilent's Advanced Design System (ADS), were used in the design of this antenna. The electromagnetic simulator in ADS is a moment-method based numerical package and is good for fast and reliable simulations. CST uses the finite difference time domain (FDTD) method, and was used to give detailed numerical predictions of input impedance, radiation patterns and radiation efficiency. The simulated input impedance of the PCB loop at 915 MHz is 5.0 + j459.4 ohms from CST, and 6.95 + j488.0 ohms from ADS.

5.1 Antenna Design Considerations

This section reviews some of the key issues encountered in the antenna design process. A combination of theoretical analysis and numerical simulations were used to optimize the design.

5.1.1 Printed Microstrip Loop versus Thin-Wire Loop

The loop considered here is made from a printed microstrip trace with a low profile rectangular cross-sectional area, whereas the bulk of the available literature considers thin-wire loops with a circular cross-sectional area.

Any conductor can be treated as an infinite depth plane conductor if two conditions are met: the cross-sectional dimensions of the conductor must be greater than the skin depth,

$$\delta = \sqrt{\frac{2}{\omega\mu\sigma}} = 2.2\mu m, \tag{5.1}$$

calculated for copper at 915 MHz, and the current must be uniformly distributed around the cross-section of the conductor [5]. The thickness of the PCB trace (20 μm) is larger than the skin depth by a factor of 10, so the first condition is satisfied. The loop thickness factor, Ω, can be estimated for this loop as

$$\Omega = 2\ln\left(\frac{p}{w/2}\right) = 8.8, \tag{5.2}$$

where p is the mean perimeter of the loop (82.4 mm) and w is the trace width (2 mm). As previously shown, the assumption of uniform current distribution for this thickness factor is marginal; however, the resulting error is not significant.

With both conditions satisfied, the internal impedance of an electrically small structure is defined as the contribution to the input impedance from fields within the conductor [5],

$$Z_s = \left(\frac{1}{\sigma\delta} + \frac{j}{\sigma\delta}\right) \times \frac{l}{w_{eff}}, \tag{5.3}$$

where l is the length of the conductor, and the effective width, w_{eff}, is illustrated below in fig. 5.4.

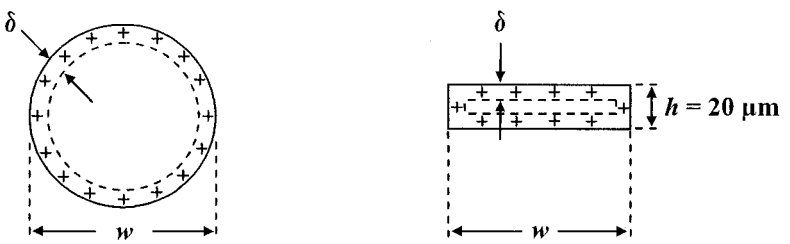

$w_{eff} = 2\pi \times w/2$ $w_{eff} \cong 2 \times w$

Thin-wire loop **PCB trace loop**

Figure 5.4: Cross-sectional area comparison between thin-wire and a PCB trace.

The ohmic loss is determined exclusively from the internal impedance. In the case where the conductor is electrically large, the non-uniform current distribution must be considered, and the ohmic loss is evaluated with the integral expression

$$P_{\Omega} = \frac{1}{\sigma \delta w_{eff}} \left[\int_{\phi=-\pi}^{\phi=-\pi} \frac{1}{2} \left| I(\phi) \right|^2 b \cdot d\phi \right]. \tag{5.4}$$

As a result, given two antennas of identical shape, one made from thin-wire and the other from a PCB trace, the latter will show higher ohmic loss by a factor of

$$\frac{P_{\Omega,PCB}}{P_{\Omega,WIRE}} = \frac{w_{eff,WIRE}}{w_{eff,PCB}} = \frac{\pi}{2}. \tag{5.5}$$

So, by using a PCB trace instead of a thin-wire the ohmic loss of the loop is increased. The penalty in terms of radiation efficiency depends on the radiation resistance, which, in turn, depends on the loop electrical size.

The input reactance of an antenna is a combination of the internal reactance (5.3) and external reactance caused by the near-fields of the antenna. For any antenna, the internal reactive component is negligible compared with the external reactance. The change in conductor shape will alter the near-fields, but the associated change in reactance should not be significant.

5.1.2 Optimum PCB Trace Width

Section 3.2 showed that small-loop theory can be used to estimate the radiation efficiency of an electrically large loop. The small loop radiation resistance,

$$R_{rad} = 20\left(\beta^2 A\right)^2, \tag{5.6}$$

is proportional to the enclosed area of the loop,

$$A = (21.2 - 2w)(24 - 2w), \tag{5.7}$$

where w is the width of the trace and all dimensions are given in mm. The area reserved for the antenna is limited to 24 mm by 21.2 mm, as shown in fig. 5.5, so the trace width can only be increased on the inside edge of the loop.

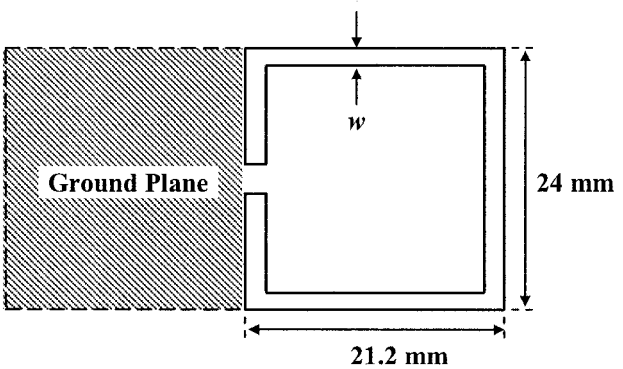

Figure 5.5: PCB antenna dimensional restrictions.

As the width of the trace is increased, the enclosed area is reduced, and radiation efficiency,

$$\eta = \frac{R_{rad}}{R_{rad} + R_{\Omega}}, \tag{5.8}$$

is also reduced.

The small loop ohmic resistance is found from the real part of (5.3).

$$R_{\Omega} = \frac{1}{\sigma\delta}\frac{p_{ave}}{2w}, \tag{5.9}$$

where the effective width, w_{eff}, is replaced with the trace width, w, as shown in fig. 5.4. The average perimeter of the loop is given by

$$p_{ave} = 2(21.2+24) - 4w. \tag{5.10}$$

So, increasing the trace width will also reduce the ohmic losses of the antenna, improving the radiation efficiency.

Section 3.1 showed that current begins to concentrate on the inside edge of the loop as the thickness factor increases. The small loop formulations used above assume a uniform circular cross-sectional current distribution, and become less accurate with increasing trace width, but still provide useful insight into the electromagnetic mechanisms.

There is a trade-off in optimizing the trace width. Increasing the width reduces ohmic loss, improving the radiation efficiency, but at the same time the enclosed area is reduced, degrading the radiation efficiency. Ultimately, the optimum trace width must be evaluated with numerical simulations. ADS is best suited for this application because the simulation has to be re-configured each time a different trace width is considered.

The FR-4 PCB substrate dissipates RF energy and is not well suited for microwave applications[3]. To evaluate the substrate loss, the simulation was repeated with the substrate loss tangent set to zero. The radiation efficiency for various trace widths, evaluated using ADS, is shown in fig. 5.6. The theoretical radiation efficiency from small loop theory is also shown.

[3] The electrical properties of FR-4 used in this simulation were a relative permittivity, ϵ_r, of 4.5 and a loss tangent, Δ, of 0.015 [48].

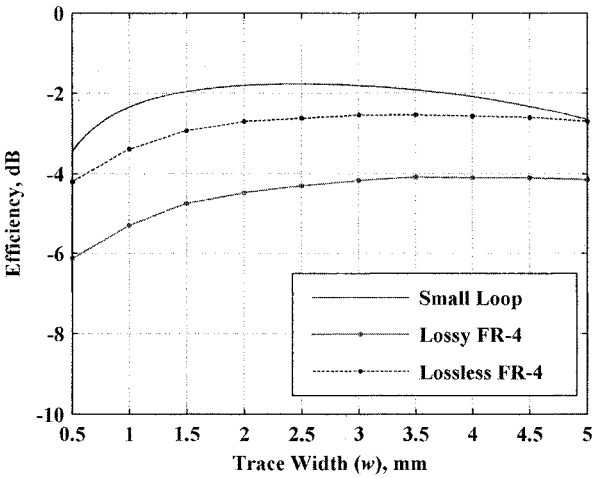

Figure 5.6: Simulated radiation efficiency versus trace width for the PCB loop (from ADS Momentum) at a frequency of 915MHz.

In this case, small loop theory predicts a higher efficiency than the numerical simulations. One possible cause of this lower simulated efficiency is concentration of current in the corners of the square loop – not accounted for in the small loop calculations.

The radiation efficiency could be slightly improved by increasing the trace width from 2mm; however, the resulting gain is not significant.

Fig. 5.6 also shows the 2 dB substrate loss is largely independent of the trace width. In hindsight, the prototype antenna should have been fabricated with a better microwave substrate.

5.1.3 Feed Structure

The most common feed structure for a loop antenna is to apply a driving potential across a small gap in the loop, but what is the appropriate gap size?

A small capacitance exists across the feed gap as shown in fig. 5.7. This capacitance, C_{gap}, can be crudely modelled as a simple parallel plate capacitor, in parallel with the input impedance of the loop, with capacitance

$$C_{gap} = \frac{\varepsilon h w}{d}, \tag{5.11}$$

where h is the trace height, d is the width of the gap, and w is the trace width. This capacitance will negatively affect the antenna by shunting current away from the radiating element (the loop).

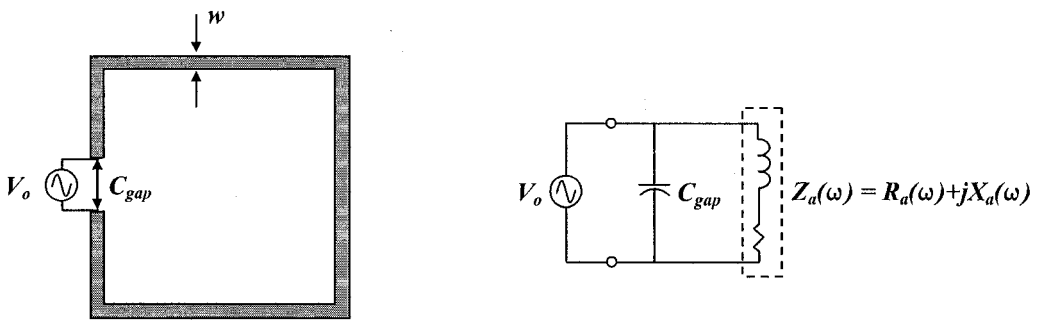

Figure 5.7: Gap-Fed loop antenna and equivalent circuit including feed-gap capacitance.

To ensure input current is delivered to the antenna, not to the gap capacitance, the reactance of the feed capacitance, X_{gap}, should be much larger than the antenna input impedance at the operating frequency, f_o,

$$\left|X_{gap}\right| = \frac{1}{2\pi f_o C_{gap}} \gg \left|Z_a\right|. \tag{5.12}$$

One advantage of the PCB loop is the extremely low height of the trace means that the above condition is satisfied for a feed gap as small as 0.1mm. For this antenna, a 2 mm gap is used because it fits well with the physical dimensions of surface mount components used in the matching network.

Finally, the loop is a symmetrically balanced antenna, and a differential voltage should be applied to maintain balanced operation.

5.1.4 Coupling with Ground Plane

At 915 MHz, the thickness of the ground plane is larger than the skin-depth of copper (5.1) by a factor of 10. Consequently, RF surface currents are induced on the ground plane, and these currents re-direct the magnetic near-field around the ground plane. This causes the ground plane to act as a reflector, distorting the radiation pattern. Additionally, the ground plane is used as a reference plane by the RF, analog, and digital electronics, so these RF currents are potentially detrimental and should be minimized.

This coupling can be reduced by increasing the distance between the ground plane and the loop; however, this can only be done by reducing the size of the loop, and in turn, the radiation efficiency of the antenna.

The tag antenna was initially simulated without the ground plane using CST, and the simulated impedance of 3.6 + j420 ohms used as a benchmark. The input impedance with the ground plane gap (distance between the loop conductor and ground plane edge) of 2 mm, previously given as 5.0 + j459.4 ohms is less than ten percent different, so the gap of 2 mm was deemed adequate.

Fig. 5.8 shows the simulated surface currents on both the ground plane and the loop. The peak surface-current on the ground plane is on the edge closest to the loop. The current density in this location is approximately ten percent of the peak current on the loop, and is 180 degrees out of phase with the current on the closest side of the loop, as is necessary to ensure the high decay of electromagnetic field components within the ground plane conductor.

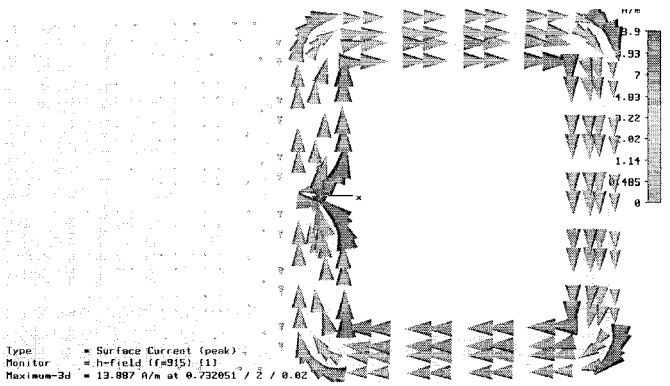

Figure 5.8: Numerically simulated surface current on both the loop antenna and ground plane. A gap-voltage excitation is used.

Fig. 5.9 shows the simulated current on the ground plane only.

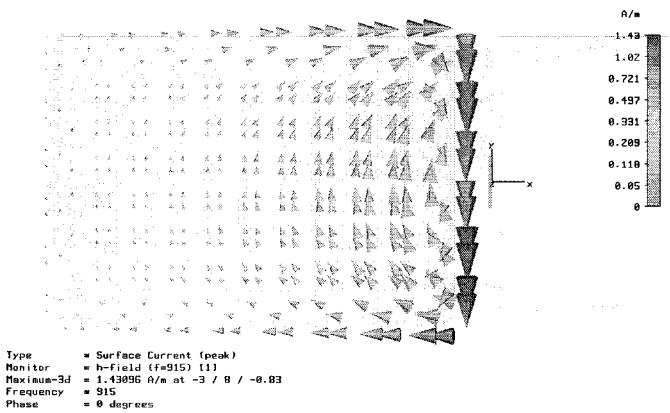

Figure 5.9: Surface current induced on ground plane.

The peak current on the right-hand edge is clearly visible, and the return current is distributed across the rest of the ground plane. Any cut in the ground plane orthogonal to this current should be avoided as this would cause localized increases in the surface current density.

5.2 Predicted Tuned Bandwidth and Radiation Patterns

CST was used to give detailed numerical predictions of input impedance, radiation patterns and radiation efficiency. The simulated input impedance versus loop electrical size is shown in fig. 5.10.

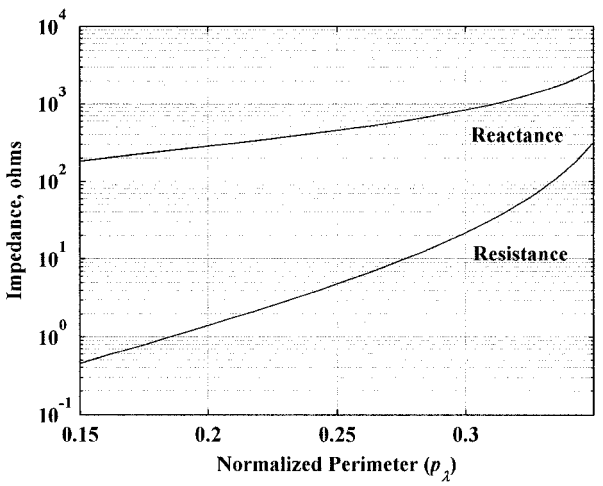

Figure 5.10: Simulated input resistance and input reactance. The lower and upper frequencies are 800 MHz and 1.0 GHz respectively.

The normalized loop perimeter at 915 MHz is approximately 0.25, where CST gives an input impedance of 5.0 +j459.4 ohms.

The quality factor of a tuned antenna, Q_z, found from the simulated input impedance as

$$Q_z(\omega) = \frac{\omega}{2R_0(\omega)}\left|Z_0'(\omega)\right|, \tag{5.13}$$

is shown in fig. 5.11 for the prototype antenna.

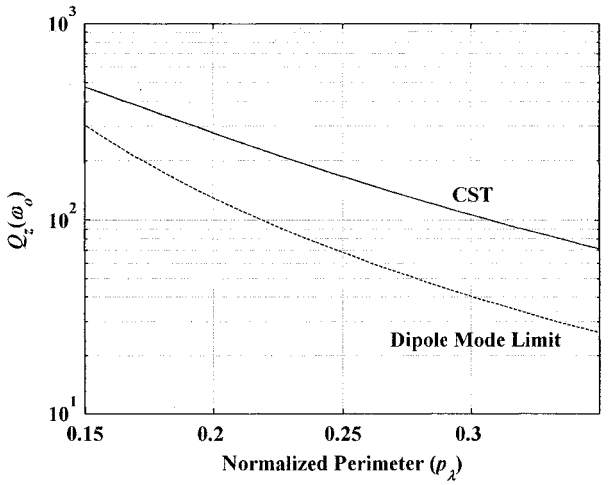

Figure 5.11: Radiation quality factor calculated using the CST generated input impedance. The Chu (single mode) limit is included for reference.

The quality factor can be used to predict the half-power fractional bandwidth of the tuned antenna

$$FBW_z \cong \frac{2}{Q_z}. \tag{5.14}$$

The radiation quality factor, from the simulated input impedance, is 164.4 at 915 MHz, the corresponding fractional bandwidth is 1.22 percent, and the absolute half-power bandwidth is 11.1 MHz.

The simulated radiation efficiency of the antenna is -3.8dB from CST, which is slightly more optimistic than the predicted -4.5dB from ADS. The CST simulation was repeated with a lossless dielectric, and the resulting efficiency is -.9dB, suggesting almost 3dB power loss in the substrate, which is more than the 2dB loss predicted by ADS. This does not include losses in the matching network, which will be considered separately.

The simulated far-field gain patterns from CST are shown in figs. 5.12 to 5.14 using a right-handed spherical coordinate system. The $G_\phi(\theta = 90°, \phi)$ pattern cut in fig. 5.12 is very close to omni-directional with a gain of about -2.5dB. This omni-directional

pattern confirms that the coupling with the ground plane is not significant enough to alter the radiation pattern of the antenna. Only the phi, ϕ, polarization is shown because the theta, θ, component is negligibly small.

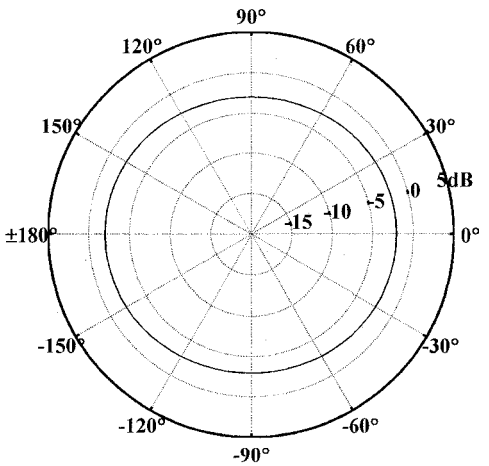

Figure 5.12: CST simulated far-field pattern $G_\phi(\theta = 90°, \phi)$ for prototype antenna.

Fig. 5.13 shows both linear polarization components: $G_\phi(\theta, \phi = 90°)$ and $G_\theta(\theta, \phi = 90°)$. The phi polarization component shows the familiar torroidal shape of the magnetic dipole (electrically small loop), and the theta polarization component has a lobe of close to -10dB on top and bottom of the loop. The electrical size of the loop, close to one-third of a wavelength, is the cause of this additional lobe, which becomes more pronounced with increasing loop electrical size.

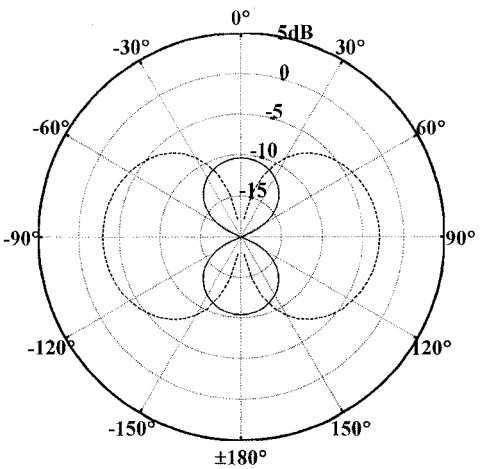

Figure 5.13: CST simulated far-field pattern for prototype antenna. The dashed line is $G_{\phi}(\theta, \phi = 90°)$ and the solid line is $G_{\theta}(\theta, \phi = 90°)$.

The $G_{\phi}(\theta, \phi = 0°)$ pattern in fig. 5.14 shows only the phi polarization component because the theta component is negligible.

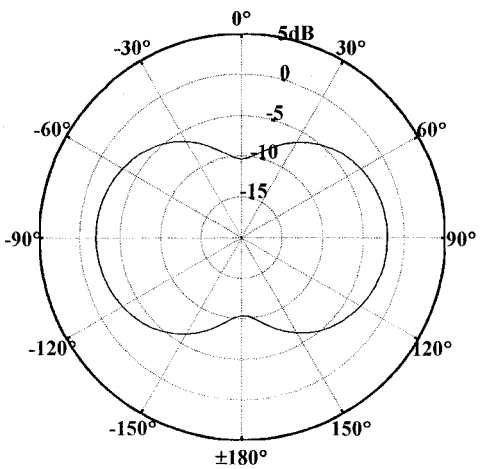

Figure 5.14: CST simulated far-field pattern cut $G_{\phi}(\theta, \phi = 0°)$ for prototype antenna.

The gain in the horizontal plane, approximately -2.5 dB, is similar to the previous patterns, and the -10 dB gain in the vertical plane is similar to the gain in the vertical plane of fig. 5.13.

5.3 Matching Network Design

The matching network topology used to match the differential (balanced) antenna impedance to a single-ended (unbalanced) fifty ohm microstrip transmission line is shown in fig. 5.15.

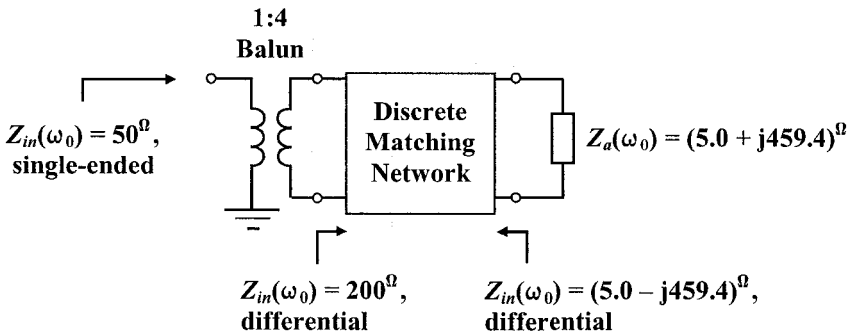

Figure 5.15: Differential to single-ended matching network.

A discrete balun[4] provides the unbalanced to balanced transformation, and also provides an impedance transform ratio of 1:4 (unbalanced 50-ohm impedance and balanced 200 ohm impedance). A balun with a 1:1 impedance transform ratio would be better suited for this application, but the 1:4 baluns were the parts on hand at the time of the design. The design of the discrete matching follows the procedure outlined in section 3.4: the single-ended equivalent is derived first and then converted to a differential scheme.

[4] Johanson Technology part number 0900BL18B200.

The first step is tuning the antenna to resonance with a series reactive element, $-jX_s = -j459.4$, as shown in fig. 5.16.

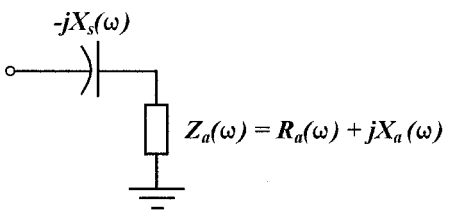

Figure 5.16: Series tuned loop antenna (single-ended).

The two-element, step-down matching network in fig. 5.16 transforms the tuned antenna input impedance, $R_a(\omega)$, to 200 ohms at the desired resonant frequency (ω_0).

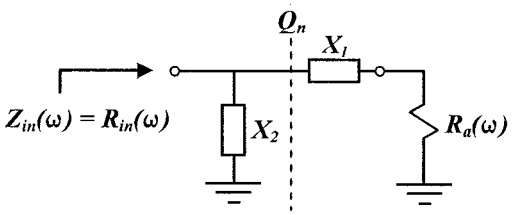

Figure 5.17: Two-element step-down matching network topology (single-ended).

The impedance transform ratio,

$$n = \frac{R_{in}(\omega_0)}{R_a(\omega_0)} = \frac{200}{5.0} = 40, \tag{5.15}$$

is used to calculate the nodal quality factor

$$Q_n = \sqrt{n-1} = 6.24. \tag{5.16}$$

The reactance values follow from the nodal quality factor and input and output resistances as

$$|X_1| = R_a Q_n = 31.2, \tag{5.17}$$

and

$$|X_2| = \frac{R_{in}}{Q_n} = 32.05. \tag{5.18}$$

The polarity of the reactance X_1 is chosen to be inductive and the polarity of reactance X_2 chosen to be capacitive.

The reactance X_1 is in series with the tuning reactance X_s. These two elements can be combined to yield an equivalent series element

$$X_{eq} = j31.2 - j459.4 = -j428.2, \tag{5.19}$$

reducing the number of elements and ohmic losses.

The resulting single-ended discrete matching network is shown in fig. 5.18.

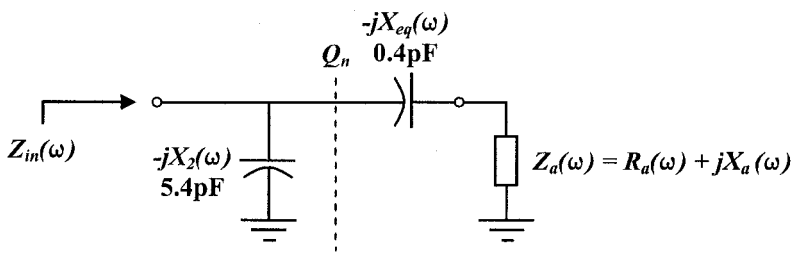

Figure 5.18: Single-ended discrete matching network.

This network is easily converted to a differential scheme by re-distributing the series reactance, X_{eq}, into two equivalent series elements on either side of the antenna as shown in fig. 5.19.

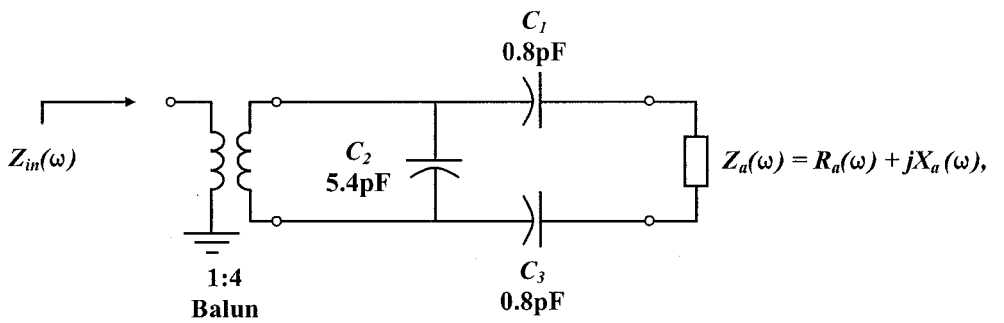

Figure 5.19: Final matching network.

This additional capacitor will increase ohmic losses, but is necessary to ensure balanced operation of the antenna.

5.3.1 Matching Network Losses

Johanson Technology provides numerical models for the capacitors and balun used in the matching network. These models were used in ADS, with the simulated antenna, to estimate the losses in the matching network. The model for the balun showed an insertion loss of 1dB at 915MHz, which agrees well with the measurements provided in the datasheet, but the models for the capacitors showed unrealistically large losses and were deemed to be inaccurate.

Appendix A contains an estimate of the losses in the capacitors calculated using ESR (equivalent series resistance) values from the capacitor datasheets. The resulting 1 dB loss in the capacitors, combined with 1 dB loss in the balun, gives a total estimated matching network loss of 2 dB.

5.4 Measurements

The surface mount balun and discrete matching network allows measurement of the antenna input impedance with a VNA. A one-port calibration sequence using discrete surface mount components as calibration standards shifts the reference plane of the network analyzer as shown in fig. 5.21. This shifted reference plane allows direct measurement of the antenna impedance. This calibration technique characterises the balun as a systematic measurement error and removes it from the measurement along with the other systematic errors.

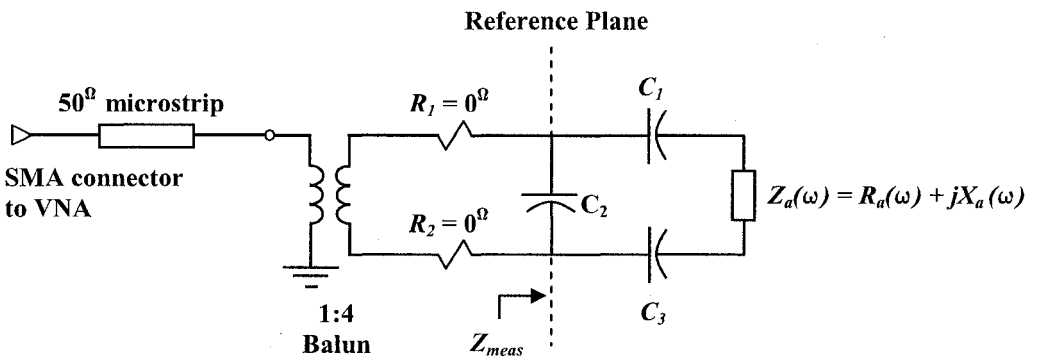

Figure 5.20: VNA measurement of antenna input impedance.

The prototype antenna includes footprints for additional series matching elements labelled R_1 and R_2. These are not needed and are populated with zero-ohm resistors.

A one-port calibration sequence requires three calibration standards: an open, a 50-ohm load, and a short. During the calibration process the footprint for C_2 is used for calibration standards, and C_2 and C_3 must be left open (unpopulated). A surface mount fifty ohm resistor is used as the fifty ohm load standard, a zero-ohm resistor as the short standard, and the pad is left unpopulated for the open standard.

Calibration standards include definitions that mathematically model the electrical characteristics of each standard. These definitions account for imperfections such as open circuit fringing capacitance and parasitic series inductance in the short standard. Surface mount components are far less ideal than proper calibration standards, so the resulting measurement accuracy is reduced; however, at the relatively low operating frequency of 915 MHz, surface mount components will still yield useful measurement data.

After calibration is complete, populating C2 and C3 with zero-ohm resistors and leaving the C1 footprint open allows direct measurement of the antenna impedance. The series impedance of the zero-ohm resistors is included in the measurement, but should not produce significant errors at 915 MHz.

There are additional limitations with this measurement technique. The antenna is not matched to the 50-ohm impedance of the measurement set-up, so the return loss is extremely high and very little power propagates through the balun to the antenna. The signal to noise ratio (SNR) of the measurement is very low, compounded by noise generated from the antenna itself. It is crucial to use the maximum available power and the noise reduction features (low IF bandwidth and time averaging) of the VNA to maximise the SNR of the measurement.

The measured antenna input impedance is shown in fig. 5.22 with the simulated input impedance from CST. The high noise of the measurement is visible in the measurement of input resistance. Although noisy, the measured impedance is clearly similar to the simulated impedance. There is a distinctive dip in the measured resistance at normalized perimeter of 0.25. This phenomenon was present in repeated measurements, and although this is the desired resonant frequency of the antenna, this measurement of the loop does not contain any tuning specific to this frequency. This irregularity is likely caused by the balun or the surface mount components used as calibration standards.

The simulated impedance diverges from the measured impedance at the upper end of the measurement, showing that the first anti-resonance of the simulated loop occurs at a slightly lower frequency than the measured loop.

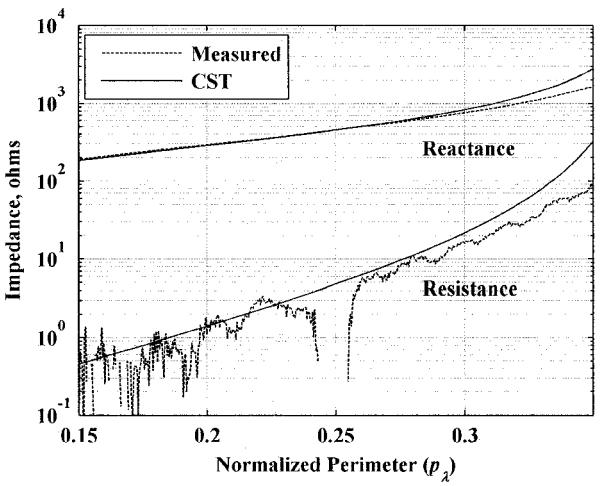

Figure 5.21: Measured loop input impedance and simulated CST input impedance.

This measurement approach is also useful for testing and tuning the matching network. By sequentially populating various components of the matching network, starting with C_1 and C_3, the nodal input impedances can be directly measured and compared with the expected nodal impedances.

Figs. 5.23 and 5.24 show the measured nodal impedances of the matching network. These measurements were taken after the component values had been manually tuned, so the component values are slightly different than theoretically calculated values.

Fig 5.23 shows the measured nodal impedance of the antenna plus the series elements. The measured impedance of 6 + j27 ohms is reasonably close to the expected impedance of 5 + j31.2 ohms.

Fig 5.24 shows the measured nodal impedance with both the series and shunt elements populated. The measured impedance of 166 + j5.3 is smaller than the expected

impedance of 200 ohms, but as long as the input impedance is close to 50 ohms, this nodal impedance is not important.

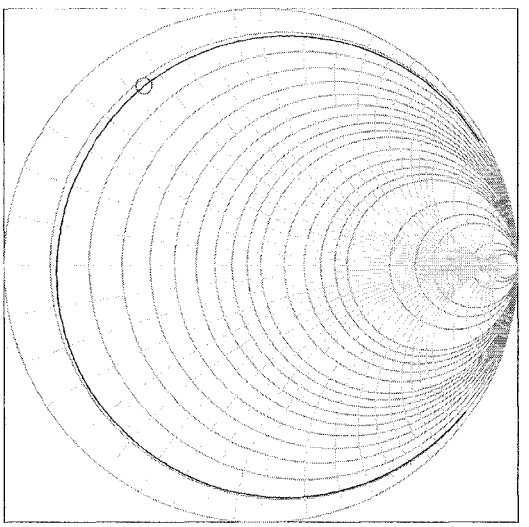

Figure 5.22: Measured nodal impedance with C_1 = 0.8pF, C_3 = 0.7pF. The nodal impedance at 915 MHz (circled) is 6 + j27 ohms.

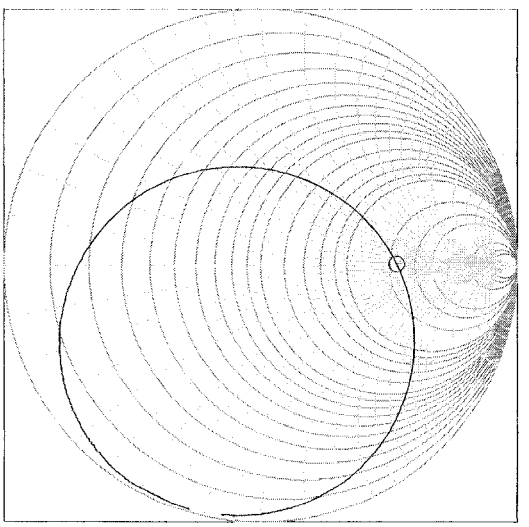

Figure 5.23: Measured nodal impedance with C_1 = 0.8pF, C_3 = 0.7pF, and C_2 = 5.0pF. The nodal impedance at 915 MHz (circled) is 166 + j5.3 ohms.

The VNA must be re-calibrated to measure the input impedance of the matching network looking into the balun. A one-port calibration with a standard calibration kit sets the VNA reference plane to the end of an SMA cable, and a port-extension equal to the electrical length of the fifty ohm microstrip line shifts the reference plane to the input of the balun. The appropriate port extension was determined experimentally as 175 psec.

This electrical delay can also be calculated using the length of the microstrip transmission line (25.5 mm) and the permittivity of the substrate. The effective dielectric constant, ϵ_{eff}, of a fifty ohm microstrip line on 32-mil FR-4 substrate is given as 3.47 [36]. The resulting phase velocity,

$$v_p = \frac{c}{\sqrt{\varepsilon_{eff}}}, \tag{5.20}$$

is used to calculate the propagation delay

$$t = \frac{d}{v_p}. \tag{5.21}$$

The theoretical calculated propagation delay is 158 psec. The additional delay in the measured value may be caused by the SMA connector.

Fig. 5.25 shows the input impedance with the VNA calibrated to the input of the balun. The measured input impedance at 915 MHz is 43.2 + j8.8 ohms, and the equivalent return loss, shown in fig. 5.26, is -18.5dB – a very good match. The lowest return loss and best impedance match is at 913 MHz; however, the resonant frequency cannot be shifted any closer to 915 MHz because of limited selection in the capacitance values of surface mount capacitors[5].

[5] Johanson Technology's S-Series ultra-low ESR capacitors were used. These are available in increments of 0.1pF.

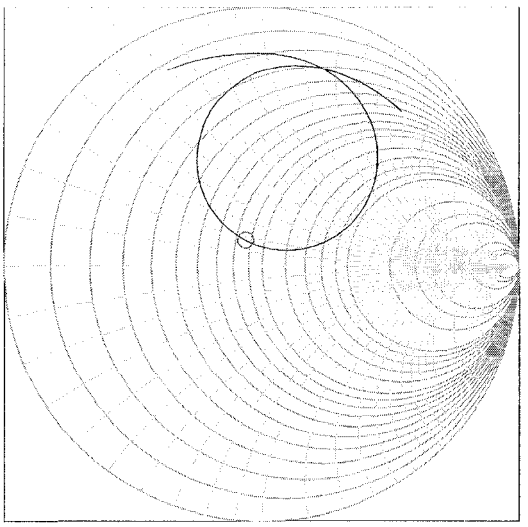

Figure 5.24: Measured input impedance of the antenna with complete matching network. The input impedance at 915 MHz (circled) is 43.2+ j8.8 ohms.

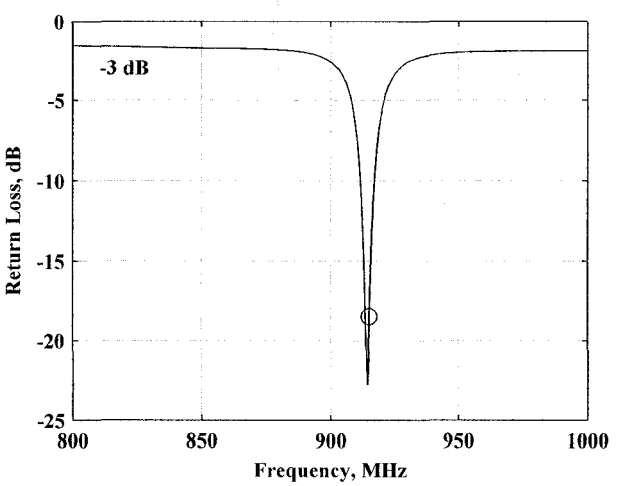

Figure 5.25: Measured return loss of the antenna with matching network. The return loss at 915 MHz (circled) is -18.5 dB.

The half-power bandwidth (-3 dB bandwidth) is approximately 24 MHz from the measured return loss. This is over twice the predicted bandwidth of 11.1 MHz. Losses in the matching network are responsible for some of this increased bandwidth, but it is unclear is there is another factor at play.

A Satimo antenna chamber[6] was used to measure the radiation efficiency and far-field patterns of the prototype antenna. To remove the matching network loss from the measurements, 2 dB has been added to the measured far-field gain patterns shown in figs. 5.27 to 5.29. The simulated antenna gain from CST is included for reference.

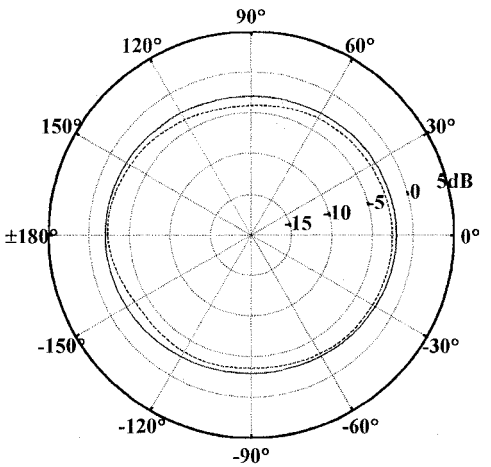

Figure 5.26: Measured (dashed line) and simulated far-field pattern $|G(\theta = 90°, \phi)|$ for the prototype antenna.

[6] Sierra Wireless provided access to their Satimo antenna chamber for the far-field gain measurements.

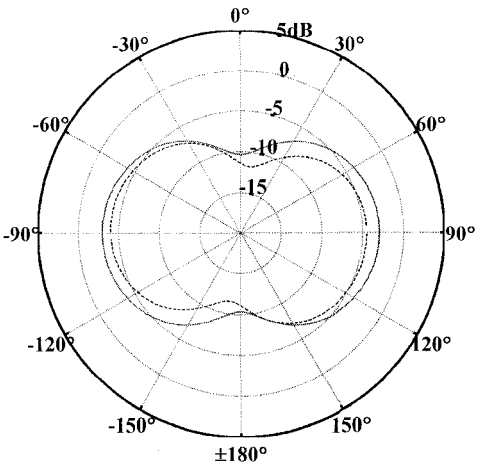

Figure 5.27: Measured (dashed line) and simulated (solid line) far-field pattern $|G(\theta, \phi = 90°)|$ for the prototype antenna.

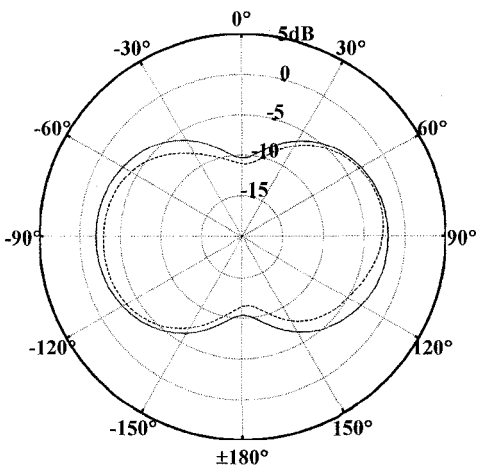

Figure 5.28: Measured (dashed line) and simulated (solid line) far-field pattern $|G(\theta, \phi = 0°)|$ for prototype antenna.

The measured radiation efficiency of the antenna and the matching network was -6.6 dB. The simulated radiation efficiency (-3.8 dB radiation efficiency) and matching loss (2 dB matching loss) was estimated as -5.8dB, so the error between the predicted and measured efficiency is less than 1 dB.

Chapter 6

Conclusions

The loop antenna can be an effective compact planar antenna, especially suited for applications in small wireless tags, and unlike many other low-profile or planar antennas, the loop antenna does not need a ground plane.

Chapter 2 reviewed previously derived solutions for the current distribution and input impedance of the electrically large thin-wire loop, and used these results to derive the theoretical radiation efficiency, not previously available, and half-power bandwidth of the tuned loop antenna. Fig. 6.1 shows the derived radiation efficiency and tuned bandwidth for a circular thin-wire loop antenna. This figure concisely summarizes the important results from this analysis: both the bandwidth and radiation efficiency improve with increasing electrical size, and a loop with normalized perimeter greater than one-half is a very efficient radiator.

A sharp anti-resonance at an electrical perimeter of approximately one-half makes impedance matching at this size exceedingly difficult, and operation in the area should be avoided. It is suggested that the optimum loop electrical size, depending on the bandwidth requirements of the system, is a normalized perimeter between one-half and one. It is possible that bandwidth demands require a further increase in electrical size, but from a radiation efficiency point of view, there is little point in using a larger loop.

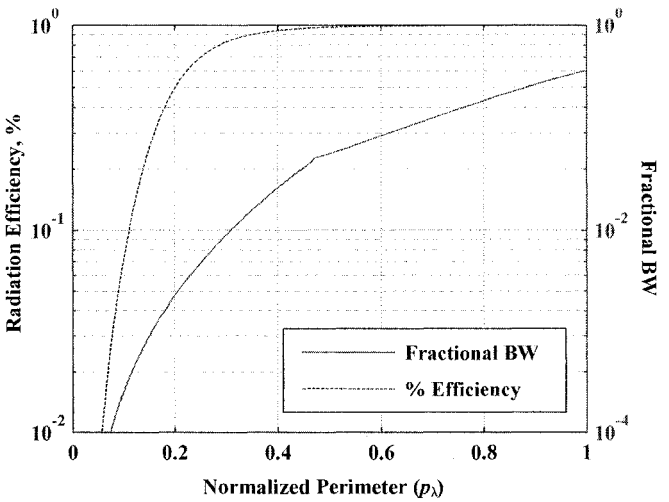

Figure 6.1: Theoretically derived radiation efficiency and maximum tuned bandwidth of a thin-wire loop antenna with radius of 20mm and loop thickness factor, Ω, of 10.

A simple approach for the design of a discrete impedance matching network was introduced, and this matching network was shown not to alter the bandwidth of the tuned loop.

Three half-loops were built and measured on an electrically large image plane, and chapter 3 showed the measured input impedance agrees well with theoretically calculated values. A Wheeler cap was used to measure the radiation efficiency of two of these loops. The measurements confirmed the theoretical trends in radiation efficiency, and the measured efficiency asymptotically approaches the theoretically predicted efficiency for the one-wavelength loop. A more accurate measurement technique is needed for confirmation of the radiation efficiency at intermediate electrical sizes.

Finally, the design and testing of a loop antenna for use in a wireless tag was presented. This design applied the theoretical results of the previous chapters, with numerical electromagnetic simulations, to design a tuned loop antenna.

Appendix A

Matching Network Loss Calculations

This appendix estimates the ohmic loss in the capacitors in this matching network shown in fig. A.1. Losses in the balun are considered separately. It should be emphasized that many simplifications are used in this analysis, and the resulting loss should be treated as a rough estimate. The carrier frequency is 915MHz, and the transmit power is 4dBm, or 2.5mW.

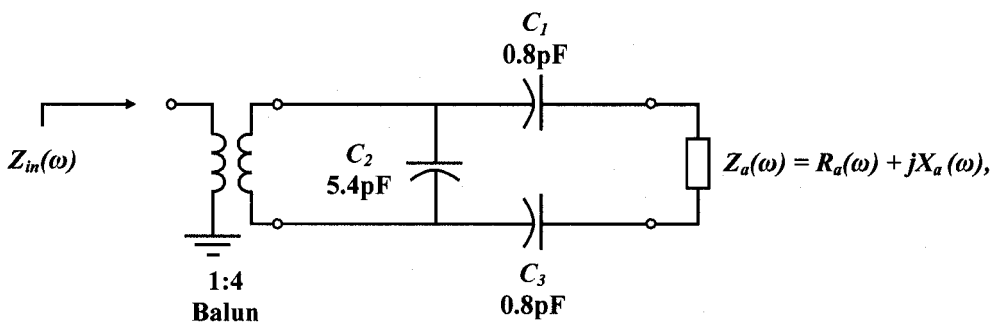

Figure A.1: Prototype antenna matching network.

First, the balun is replaced with an ideal voltage source delivering 2.5mW of power into a resistive load of 200 ohms,

$$V_0 = \sqrt{P_{out} R_{in}} = .707v, \tag{A.1}$$

as shown in fig. A.2.

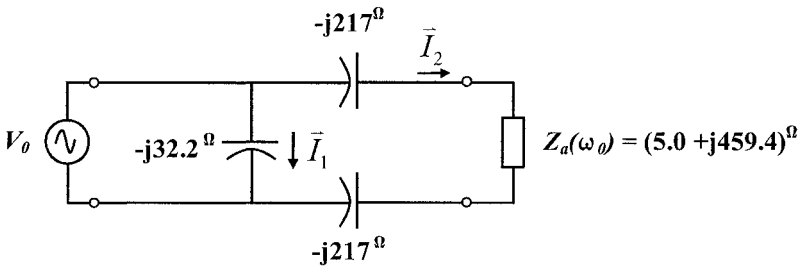

Figure A.2: Prototype antenna matching network.

The capacitors are treated as ideal (lossless) to facilitate calculation of the currents in the matching network,

$$\vec{I}_1 = \frac{V_{out}}{-j32.2} = 22.0\angle 90°mA, \tag{A.2}$$

$$\vec{I}_2 = \frac{V_{out}}{2(-j217)+(5+j459.4)} = 27.3\angle -78.9°mA. \tag{A.3}$$

The effective series resistance (ESR) of the capacitors, given as one-tenth of an ohm at 915MHz[7], is needed to calculate the ohmic losses,

$$P_{CAP} = \sum I^2 R = .1^{\Omega}\left[(22.0mA)^2 + 2(27.3mA)^2\right] \simeq 0.2mW. \tag{A.4}$$

Finally, the power delivered to the antenna,

$$P_{ANT} = 2.5mW - 0.2mW = 2.3mW, \tag{A.4}$$

is used to find a rough estimate of the efficiency of the matching network,

$$\eta = \frac{P_{ANT}}{P_{IN}} = \frac{2.3mW}{2.5mW} = 92\%, \tag{A.5}$$

or alternatively in dB form,

[7] Johanson Technology's S-Series ultra-low ESR capacitors.

$$\eta_{dB} = 10\log(\eta) = -.4dB. \tag{A.6}$$

This estimate should be rounded down to at least -1 dB to provide some margin of error, given the approximate nature of the calculation.

Bibliography

[1] H. C. Pocklington, "Electrical oscillations in wires,'' *Proc. Cambridge Phys. SOC.*, vol. 9, pp. 324-333, 1897.

[2] J. D. Kraus, R. J. Marhefka, *Antennas for All Applications.* Third Edition, McGraw Hill, New York, 2002.

[3] W.L. Stutzman, G.A. Thiele, *Antenna Theory and Design.* John Wiley and Sons, New York, 1981.

[4] A.B. Balanis, *Antenna Theory, Analysis and Design.* Third Edition, John Wiley and Sons, New York, 2005.

[5] S. Ramo, J. R. Whinnery, T. Van Duzer, *Fields and Waves in Communications Electronics.* John Wiley and Sons, New York, 1965.

[6] E. Hallen, "Theoretical investigation into transmitting and receiving qualities of antennae," *Nova Acta Regiae SOC. Ser. Upps.*, vol. II, pp. 1 4 , Nov. 4, 1938.

[7] J. E. Storer, "Impedence of thin-wire loop antennas," *Trans. AIEE*, vol. 75, pp. 606-619, Nov. 1956.

[8] P. A. Kennedy, "Loop antenna measurements," *IEEE Trans. Antennas Propagat.*, vol. AP-4, pp. 610-618, Oct. 1956.

[9] T. T. Wu, "Theory of the Thin Circular Loop Antenna," *Journal of Mathematical Physics*, vol. 3, pp. 1301-1304, Nov. – Dec. 1962.

[10] C.-L. Chen, R. W. P. King, "The small bare loop antenna immersed in a dissipative medium," *IEEE Trans. Antennas Propagat.*, vol. AP-11, pp. 266-269, May 1963.

[11] R. W. P. King, C. W. Harrison Jr., D. G. Tingley, "The admittance of bare circular loop antennas in a dissipative medium," *IEEE Trans. Antennas Propagat.*, vol. AP-12, pp. 434-438, July 1964.

[12] R. W. P. King, C. W. Harrison Jr., D. G. Tingley, "The current in bare circular loop antennas in a dissipative medium," *IEEE Trans. Antennas Propagat.*, vol. AP-13, pp. 529-531, July 1965.

[13] R. W. P. King, *Antenna Theory, Part 1.* Chapter 11, R. E. Collin and F. J. Zucker editors, McGraw-Hill, New York, 1969.

[14] G. S. Smith, "A note on the imperfectly conducting circular-loop antenna," *Radio Science Journal*, vol. 8, pp. 711–725, July 1973.

[15] G. S. Smith, "On the electrically small bare loop antenna in a dissipative medium," IEEE *Trans. Antennas Propagat.*, vol. AP-24, pp. 533-537, July 1976.

[16] R. W. P. King, G. S. Smith, *Antennas in Matter: Fundamentals, Theory and Applications.* MIT Press, Cambridge, MA, 1981.

[17] Q. Balzano, K. Siwiak, "The near field of annular antennas," *IEEE Trans. Vehicular Tech.*, vol. VT-36, pp. 173-183, Nov. 1987.

[18] G. Zhou, G. S. Smith, "An accurate theoretical model for the thin-wire circular half-loop antenna," *IEEE Trans. Antennas Propagat.*, vol. AP-39, pp. 1167-1177, Aug. 1991.

[19] J.B. Sherman, "Circular loop antennas at ultra-high frequencies," *Proc. IRE*, vol. 32, pp. 534-537, Sept. 1944.

[20] G. Glinski, "Note on the circular loop antennas with non-uniform current distribution," *J. Appl. Phys.*, vol. 18, pp. 638–644, July 1947.

[21] E. J. Martin, Jr., "Radiation fields of circular loop antennas by a direct integration process," *IEEE Trans. Antennas Propagat.*, vol. AP-8, pp. 105–107, Jan. 1960.

[22] J. E. Lindsay, Jr., "A circular loop antenna with non-uniform current distribution," *IEEE Trans. Antennas Propagat.*, vol. AP-8, pp. 439–441, July 1960.

[23] B. R. Rao, "Far-field patterns of large circular loop antennas: Theoretical and experimental results," *IEEE Trans. Antennas Propagat.*, vol. AP-16, pp. 269–270, Mar. 1968.

[24] D. H. Werner, "An exact integration procedure for vector potentials of thin circular loop antennas," *IEEE Trans. Antennas Propagat.*, vol. AP-44, pp. 157–165, Feb. 1996.

[25] L. W. Li, M. S. Leong, P. S. Kooi, T. S. Yeo, "Exact solutions of electromagnetic fields in both near and far zones radiated by thin circular-loop antennas: a general representation," *IEEE Trans. Antennas Propagat.*, vol. AP-45, pp. 1741–1748, Dec. 1997.

[26] L.W. Li, C.P. Lim, and M.S. Leong, "Method-of-moments analysis of electrically large circular loop antennas: Non-uniform current," *Proc. Inst. Elect. Eng. Microw. Antennas Propag.*, vol. 146, pp. 416–420, 1999.

[27] L.W. Li, S. Krishnan, M.S. Leong, P. S. Kooi, "Radiation Q of electrically large loop antennas with non-uniform currents," *Microwave and Optical Technology Letters*, vol. 34, pp. 377-380, Sept. 2002.

[28] J.T. Conway, "New exact solution procedure for the near fields of the general thin circular loop antenna," *IEEE Trans. Antennas Propagat.*, vol. AP-53, pp. 509-517, Jan. 2005.

[29] A.D. Yaghjian, S.R. Best, "Impedance, bandwidth, and Q of antennas," *IEEE Trans. Antennas Propagat.*, vol. AP-53, pp. 1298-1324, Apr. 2005.

[30] A.D. Yaghjian, S.R. Best, "The lower bounds on Q for lossy electric and magnetic dipole antennas," *IEEE Antennas Wireless Propag. Lett.*, vol. 3, pp. 314-316, 2004.

[31] J. S. McLean, "A re-examination of the fundamental limits on the radiation Q of electrically small antennas," *IEEE Trans. Antennas Propagat.*, vol. AP-44, pp. 672-676, May 1996.

[32] R. C. Hansen, "Fundamental limitations in antennas," *Proc. IEEE*, vol. 69, pp. 170-182, Feb. 1981.

[33] H. A. Wheeler, "Fundmental limitations of small antennas," *Proc. IRE*, vol. 35, pp. 1479-1484, Dec. 1947.

[34] L. J. Chu, "Physical limitations on omni-directional antennas," *J. Appl. Phys.*, vol. 19, pp. 1163-1175, Dec. 1948.

[35] "Impedance matching networks applied to RF power transistors," *Motorola application note AN721*, 1993.

[36] R. Ludwig, P. Bretchko, *RF Circuit Design: Theory and Applications*. Prentice Hall, New Jersey, 2000

[37] G. Gonzales, *Microwave Transistor Amplifiers, Analysis and Design.* Second Edition, Prentice Hall, New Jersey, 1997

[38] R. Vaughan, J.B. Andersen, *Channels, Propagation and Antennas for Mobile Communications.* The Institution of Electrical Engineers, London, 2003.

[39] H. A. Wheeler, "The radiansphere around a small antenna", *Proc. IRE*, vol. 47, pp. 1325 – 1331, Aug. 1959

[40] E. H. Newman, P. Bohley, and C. H. Walter, "Two methods for the measurement of antenna efficiency," *IEEE Trans. Antennas Propagat.*, vol. AP-23, pp. 457-461, July 1975.

[41] D. M. Pozar, B. Kaufman, "Comparison of three methods for the measurement of printed antenna efficiency," *IEEE Trans. Antennas Propagat.*, vol. 36, pp. 136-139, Jan. 1988.

[42] G. S. Smith, "An analysis of the wheeler method for measuring the radiating efficiency of antennas," *IEEE Trans. Antennas Propagat.*, vol. 25, pp. 552-556, Jul. 1977.

[43] D.K. Cheng, *Field and Wave Electronics, Second Edition*. Addison Wesley, New York, 1992.

[44] R. S. Elliot, *Electromagnetics*. McGraw Hill, New York, 1966.

[45] J. D. Kraus, *Electromagnetics.* Fourth Edition, McGraw Hill, New York, 1992.

[46] G.S. Smith, *An Introduction to Classical Electromagnetic Radiation.* Cambridge University Press, Cambridge, 1997.

[47] *Antenna Engineering Handbook.* Third Edition, R.C. Johnson, editor, McGraw Hill, New York, 1993, in particular Ch.5: Loop Antennas, G.S. Smith, and Ch. 6: Small Antennas, H.A. Wheeler.

[48] J.R. Aguilar, M. Beadle, P.T. Thompson, M.W. Shelley, "The microwave and RF characteristics of FR4 substrates," *IEE Colloquium on Low Cost Antenna Technology*, pp. 2/1-2/6, Feb. 1998.

[49] S. Adachi, Y. Mushiaki, "Theoretical formulation for circular loop antennas by integral equation method," *Sci. Rep. RITU*, vol. 9, pp. 9-18, 1957.

[50] S. Adachi, Y. Mushiaki, "Studies of large circular loop antennas," *Sci. Rep. RITU*, vol. 9, pp. 79-103, 1957.

[51] S. Adachi, Y. Mushiaki, "Directive loop antenna," *Sci. Rep. RITU*, vol. 9, pp. 105-112, 1957.

[52] T. Kasahara, S. Adachi, and Y. Mushiake, "Calculation of the impedances of impedance-terminated loop antennas by the EMF method," *Electronics and Communications in Japan (IECE of Japan Trans.)*, vol. 52, pp 73-80, 1969.